
Satellite Products and Services Review Board

**Algorithm Theoretical
Basis Document
for NOAA NDE OMPS
Version 8 Total Column Ozone (V8TOz)
Environmental Data Record (EDR)
Version 1.0**



TITLE: FOR NOAA NDE OMPS VERSION 8 TOTAL COLUMN OZONE

AUTHORS:

Lawrence Flynn NOAA STAR

Zhijia Zhang (IMSG)

Valerie Mikles (IMSG)

Bigyani Das (IMSG)

Jianguo Niu (SRG)

C. Trevor Beck (STAR)

Eric Beach (IMSG)

APPROVAL SIGNATURES:

Lihang Zhou (STAR) March 12, 2016
STAR JPSS Lead Date

Remarks: This document shares algorithm descriptive material with the corresponding NASA-sponsored Version 8 Total Column Ozone algorithm theoretical basis document.

**DOCUMENT HISTORY
DOCUMENT REVISION LOG**

The Document Revision Log identifies the series of revisions to this document since the baseline release. Please refer to the above page for version number information.

DOCUMENT TITLE: Algorithm Theoretical Basis Document Template			
DOCUMENT CHANGE HISTORY			
Revision No.	Date	Revision Originator Project Group	CCR Approval # and Date
1.0	3/1/2015	L. Flynn	
1.1	3/10/2017	L. Flynn	

TABLE OF CONTENTS

	<u>Page</u>
LIST OF TABLES AND FIGURES.....	8
1. INTRODUCTION.....	9
1.1. Product Overview.....	9
1.1.1. Product Description.....	9
Product History.....	9
1.1.2. Product Requirements.....	10
1.2. Satellite Instrument Description.....	10
2. ALGORITHM DESCRIPTION.....	11
2.1. Processing Outline.....	11
2.2. Algorithm Input.....	21
Input Satellite Data.....	21
Satellite Data Preprocessing Overview.....	21
Input satellite data description.....	22
Input Ancillary Data – Climatology and RT LUTs.....	22
2.3. Theoretical Description.....	23
2.3.1. Physical Description.....	23
2.3.2. Mathematical Description.....	30
2.4.2 Inverse Model Errors.....	45
O ₃ Profile.....	45
Temperature Profile.....	46
2.4.3 Instrumental Errors.....	47
Spectral Calibration.....	47
Radiometric Calibration.....	47
Instrument Noise.....	47
2.4.4 Error Summary.....	47
2.4. Algorithm Output.....	2
2.5. Performance Estimates.....	5
2.5.1. Test Data Description.....	5
2.5.2. Sensor Effects.....	5
2.5.3. Retrieval Errors.....	7
2.5.4. Numerical Computation Considerations.....	8
2.5.5. Programming and Procedural Considerations.....	8
2.5.6. Quality Assessment and Diagnostics.....	8
2.5.7. Exception Handling.....	8
2.6. Validation.....	8
3. ASSUMPTIONS AND LIMITATIONS.....	9
3.1. Performance Assumptions.....	9

3.2. Potential Improvements..... 9

4. REFERENCES 10

LIST OF TABLES AND FIGURES

Table 2-1: List of input data sets used in the VIIRS AF algorithm. All input data sets have a nominal resolution of 750 m..... **Error! Bookmark not defined.**

Table 2-2: VIIRS AF science data sets. Variable n indicates the number of 48-scan blocks found in a single granule ($n=1$ for NDE granule) (see Section 1.1.1).**Error! Bookmark not defined.**

Figure 1-1: VIIRS AF fire mask (native swath projection) over an area in Northern Canada derived from a VIIRS granules acquired approximately at 20:06 UTC on 29 May 2015. **Error! Bookmark not defined.**

Figure 2-1: VIIRS AF algorithm processing flow. Input data are gathered (SDR) and pre-processed (granulation of land/water mask), and ingested into the fire detection module for scan i along with scan $i-1$ and $i+1$ used in the contextual analyses. Finally FRP is calculated for each fire pixel detected.20

Figure 2-2: Spectral radiance for average land, flaming, and smoldering fire temperatures, and the spectral response functions of all six VIIRS channels used by the Active Fire Algorithm. **Error! Bookmark not defined.**

Figure 2-3: Percentage of M15 aggregated pixels resulting from the mixing of saturated and un-saturated native pixels. Results were generated using simulated VIIRS data based on actual Advanced Spaceborne Thermal Emission and Reflection Radiometer (ASTER) 30-m resolution fire-affected pixels.**Error! Bookmark not defined.**

Figure 2-4: Spectral response functions for VIIRS I4 and M13, and MODIS B21/22 mid-infrared channels, and the corresponding atmospheric transmittance calculated using MODTRAN assuming U.S. standard atmospheric conditions (top panel). Bottom panel shows the corresponding net atmospheric absorption as a function of scan angle. **Error! Bookmark not defined.**

Figure 2-5: S-NPP/VIIRS AF and Aqua/MODIS MYD14 fire detection data produced for the King fire/California on 14-19 September 2014.**Error! Bookmark not defined.**

Figure 2-6: Validation of VIIRS AF active fire pixels (marked in thick dashed lines) using airborne reference fire data (background color image, active fires in yellow-red shades) during the Prescribed Fire Combustion and Atmospheric Dynamics Research (RxCADRE) experiment at Eglin Air Force Base/FL, 10 November 2012. **Error! Bookmark not defined.**

1. INTRODUCTION

This document presents the scientific background, design and performance of the Ozone Mapping and Profiler Suite Nadir Mapper (OMPS NM) Version 8 Total Column Ozone (V8TOz) Environmental Data Record (EDR) algorithm for the Joint Polar Satellite System (JPSS). The V8TOz algorithm produces a bundled set of outputs from OMPS NM measurements of Backscattered Ultraviolet (BUV), including the following: (i) Total Column Ozone estimates; (ii) an Absorbing Aerosol Index; (iii) Effective BUV Reflectivity, and (iv) measurement sensitivities and residuals.

Products from the OMPS V8TOz algorithm described here fulfill the requirements identified in the JPSS OMPS Total Column Ozone. Furthermore, those requirements provide continuity to the NASA EOS Aura Ozone Monitoring Instrument (OMI).

1.1. Product Overview

1.1.1. Product Description

Product description with sufficient detail so that the user understands how to use the product files. (*Document Object 34*)¹

Writers: Algorithm Scientists.

The NDEV8T provides the Ozone Mapping and Profiler (OMPS) Total Column Ozone bundled product as created by the Version 8 Total Ozone retrieval algorithm developed at NASA GSFC. The work to transition the algorithm to NOAA operations was completed as part of the NOAA JPSS Product Development, Calibration and Validation program led by the NOAA NESDIS Center for Satellite Applications and Research (STAR). It will be delivered to the Suomi NPP Data Exploitation (NDE) team and integrated into the NDE Data Handling System (DHS) where it will be run in a pre-operational manner. After a preliminary testing period, the NDE DHS will, in turn, be delivered to the Office of Satellite and Product Operations (OSPO) to be run operationally.

The NDEV8T product was developed to generate Total Column Ozone estimates from a discrete set of 12 measurements of backscattered ultraviolet radiances in the 308 nm to 380 nm range. In addition to the total ozone estimates, it produces effect UV reflectivity, absorbing aerosol index values and retrieval information such as measurement sensitivities and residuals and retrieval efficiency factors. The algorithm processes all daytime OMPS Nadir Mapper Sensor Data Records (SDRs) pixels globally. Details on the content of the NDEV8T external output files are provided in the product output section.

Product History

The NDEV8T is a new implementation of the Version 8 Total Column Ozone developed by NASA GSFC for the Total Ozone Mapping Spectrometer (TOMS) series of instruments and refined for use with the NASA EOS Aura Ozone Monitoring Instrument (OMI). NOAA has

previously implemented this algorithm operationally to create products from measurements made by the EUMETSAT Global Ozone Monitoring Experiment (GOME-2) instruments. This product replaces the current operational IDPS Total Column Ozone IP an EDR products (INCTO and OOTCO). The IDPS product meets the JPSS Level 1 requirements with the exclusions applicable for Suomi-NPP only. The new product will couple with the Linear Fit SO₂ algorithm to provide corrections to the total column ozone estimates for elevated atmospheric SO₂ amounts. It will also be consistent with the existing NOAA GOME-2 and NASA TOMS/OMI records.

1.1.2. Product Requirements

State the requirements for each product, either explicitly or by reference to the project's requirements document, if available. Product requirements should include content, format, latency, quality. (*Document Object 1*)

Writers: Development Lead.

All NDEV8TOz basic and derived requirements are available in the NDEV8T Requirements Allocation Document (RAD). These requirements identify the users and their needs with respect to file content, format, latency, and quality. They are based on the Level 1 Requirements for Total Column Ozone EDRs from the JPSS program.

1.2. Satellite Instrument Description

Describe the attributes of the sensing system(s) used to supply data for the retrieval algorithm at a level of detail sufficient for reviewers to verify that the instrument is capable of supplying input data of sufficient quality. (*Document Object 28*)

Writers: Development Lead and PAL should collaborate.

The Ozone Mapping and Profiler Suite (OMPS) is the next-generation Joint Polar Satellite System (JPSS) US ozone monitoring system. The OMPS is designed to continue the measurements of both the NASA Total Ozone Mapping Spectrometer (TOMS) and NOAA Solar Backscatter Ultraviolet Spectrometer/2 (SBUV/2) systems. The OMPS has two instrument modules: a combined Nadir Mapper and Nadir Profiler, and a separate Limb Profiler.

The OMPS was designed to meet the stringent set of performance requirements for atmospheric ozone products detailed in the JPSS System Requirements Document. The OMPS Nadir Mapper measurement capabilities were developed to give performance at least as good as the requirements in Section 3.4.5.2 Ozone Total Column Product Requirements of the Joint Polar Satellite System (JPSS) Data Product Specification.

Both nadir sensors are designed to make measurements of the ultraviolet radiance backscattered by the Earth's atmosphere and surface (BUV) and of the extra-terrestrial solar irradiance. The radiance/irradiance ratios are the principal quantities used in the ozone retrieval algorithms. The sensor detectors are 2-dimensional Charge-Coupled Devices (CCDs) arrays with spatial (cross-track) and spectral dimensions. The detectors are actively cooled to reduce dark currents and radiation damage. Each of the nadir spectrometers samples the spectrum at 0.42 nm with 1-nm Full-Width-Half-Maximum (FWHM) end-to-end resolution.

Long-term calibration stability is maintained by periodic solar observations using a Working and Reference reflective diffuser system similar to the system successfully deployed on the recent TOMS sensors.

The total column sensor has a 110° cross-track FOV and 0.27° along-track slit width. The OMPS Nadir Mapper is highly flexible in its operations and can be used to provide a range of spatial resolution by exercising less on-board binning. The SDR algorithm is designed to handle the full range of spatial resolution measurements and create products with nadir resolution from 50 km to 17 km. In low-resolution mode, the CCD array pixels are summed into 35 cross-track bins (with approximately 20 spatial pixels in each bin). These are 3.35° (50 km) at nadir and 2.84° at ±55° (120 km). The resolution in this mode is 50 km along-track at nadir with a 7.6-Second reporting period. In medium resolution mode, there are 105 cross-track FOVs, 17 km at nadir and the 17 km along track with a 2.5-Second reporting period. The spectral coverage is from 300 nm to 420 nm, with the signal shared with the nadir profiler between 300 nm and 310 nm through the use of a dichroic beam splitter.

(Document Object 28)

2. ALGORITHM DESCRIPTION

The NDEV8 product is generated from the Version 8 Total O₃ algorithm (V8TOz). The Version 8 total O₃ algorithm (V8TOZ) is the most recent version of a series of BUUV (backscattered ultraviolet) total O₃ algorithms that have been developed since the original algorithm proposed by *Dave & Mateer [1967]*, which was used to process Nimbus-4 BUUV data [*Mateer et al., 1971*]. The algorithm makes two key assumptions about the nature of the BUUV radiation. Firstly, we assume that the BUUV radiances at wavelengths greater than 310 nm are primarily a function of total O₃ amount, with only a weak dependence on O₃ profile that can be accounted for using a set of standard profiles. Secondly, we assume that a relatively simple radiative transfer model that treats clouds, aerosols, and surfaces as Lambertian reflectors can account for most of the spectral dependence of BUUV radiation, though corrections are required to handle special situations. The algorithm uses measurements at 12 channels to estimate the effective reflectivity and create absorbing aerosol and SO₂ indices. A radiative transfer lookup table created using standard ozone profiles is used to match the viewing conditions and an ozone absorbing channel measurement. The Version 8 algorithm has incorporated procedures for identifying the special situations, and apply semi-empirical corrections, based on accurate radiative transfer models, to minimize the errors that occur in these situations.

2.1. Processing Outline

Full description of the processing outline of the retrieval algorithm. All key elements and sub-elements needed to convey a comprehensive sense of the algorithm should be included. The level of detail should be consistent with the current maturity of the software architecture (which will improve with each revision). A data flow diagram consistent with the software architecture is preferred. *(Document Object 13)*

Writers: Algorithm Scientists.

The OMPS V8TOz is a self-contained algorithm with no dependencies on other Level 2 products. It reads input OMPS Sensor Data Record (SDR) and Geolocation Data Records (GEO) and combines these with climatological and radiative transfer lookup table (RTLUT)

input to generate the Total Column Ozone estimates. All OMPS Earth View SDRs on the dayside of the orbit are processed individually.

Description modules of NDE-V8TOZ algorithm:

Climatology_class

This module reads in climatological data of terrain pressure information; cloud pressure information for 12 months; snow/Ice index information for 12 months, and interpolates the monthly values into a particular day.

O3T_apriori_class

This module reads in a priori ozone profile for a given day and latitude, and interpolates a priori ozone profile based on Julian date and latitude.

O3T_class

This module contains the functions that implement the algorithm steps in the process of successive improvement of ozone retrieval.

O3T_const

This module stores a number of constants used to be in data file CONST.EP, CONST.N7, CONST.M3 of the V8TOZ codes.

O3T_dndx_class

This module reads in tables for calculation of forward model quantities: dN/dX , and dN/dT .

O3T_dndx_m

This module computes dndx for selected lambdas for a given table pressure, profile, albedos, zenith angle and scan angle.

O3T_input_class

This module contains the functions that read in the namelist from control file and read in geo/sdr data from IDPS outputs.

O3T_irrad_class

This module is used for handling SDR data; currently its main function is moved to module O3T_omps and O3T_input_class.

O3T_iztrsb_m

This module contains function for forward calculation of the components that made up the nvalue.

O3T_lpolycoef_class

This module contains a set of functions to calculate the coefficients used in Lagrangian interpolation.

O3T_lpolyinterp_class

This module contains functions that perform the Lagrange interpolation of the N-value components.

O3T_nval_class

This module reads in tables for calculation of forward model quantity: n-value.

O3T_omps

This is the main program that implements the three-step process of successive improvement of the estimation of total column amount ozone.

O3T_output_class

This module contains the functions that output ozone retrievals in NetCDF and HDF5 files

O3T_pixel_class

This module defines the pixel geo-angle data type (O3T_pixgeo_type) and pixel surface cover type (O3T_pixcover_type) and makes module O3T_pixel_class.mod. In addition, a set of functions to set the field values of these data types.

O3T_radgeo_class

This module contains the allocatable arrays used to store in GEOlocation information and Earth view RADIance information from the input data file.

O3T_so2_class

This module computes the SO₂ index from residues and pre-stored coefficients for OMI, GOMI, and for the different TOMS instruments on different satellite platforms.

O3T_stnprof_class

This module contains the standard O₃ profiles used in the master Look-Up Table calculations.

UTIL_mmddInterp_class

This module is for handling year, month, and day.

UTIL_tools_class

This module is used for handling data; calculating weights; performing linear interpolation.

The subroutines/functions for the NDE-V8TOZ algorithm:

getFileName

This function is for reading in file names from control file.

get_index

This subroutine returns the index that has minimum value of the input array.

hunt

Given an array $xx(1:N)$, and given a value x , returns a value jlo such that x is between $xx(jlo)$ and $xx(jlo+1)$. xx must be monotonic, either increasing or decreasing. $jlo = 0$ or $jlo = N$ is returned to indicate that x is out of range. jlo on input is taken as the initial guess for jlo on output.

pixGetTerPres

This subroutine reads in climatological terrain pressure information.

pixGetCldPres

This subroutine reads in climatological cloud pressure information for 12 months.

pixGetSnowIce

This subroutine reads in climatological snow/Ice index information for 12 months.

mmddInterp

This subroutine interpolates the monthly values (snow/ice, cloud pressure) into a particular day.

O3_so2_index

This subroutine computes SO2 index from residues and pre-stored coefficients for specified instruments, such as GOME-2.

O3_so2_setCoef

This subroutine reads in pre-stored coefficients for calculating SO2.

O3T_apriori_prf

This subroutine determines a priori temperature profile, given latitude and Julian day.

O3T_apriori_rd

This subroutine reads in a priori ozone profile for a given day and latitude

O3T_blwclld

This subroutine calculates ozone amount beneath cloud for various cloud scenario: partially clouded, fully clouded, lower, and high clouded situations.

O3T_calcRefl

This subroutine uses the interpolation indices for table lookup, and performs table interpolations in pressure and ozone, assumed ground and cloud reflectivity, then calculates cloud fraction. It checks for the presence of snow or sun-glint, for which clear sky is assumed. It calculates reflectivity by inverting the surface radiance formula for clear or completely cloudy, and uses the partial cloud model for partly clouded scenes.

O3T_delnbyT

This subroutine computes the Jacobian $\frac{dN}{dT}$ for each of 11 Umkehr layers and all the selected wavelengths using a chain rule relating $\frac{dN}{dT}$ to $\frac{dN}{dX}$, where X is layer ozone amount.

O3T_dndomega

This subroutine computes sensitivity $\frac{dN}{d\Omega}$.

O3T_dndx

This subroutine performs a table lookup on quantities i_0, i_1, i_2 , using pre-computed Lagrangian polynomial coefficients interpolates table values to evaluate quantities for current θ_0 and θ .

O3T_dndx_setup

This subroutine reads in tables for calculation of forward model quantities: $\frac{dN}{dX}$ and $\frac{dN}{dT}$.

O3T_getLambdaSet

This subroutine reads in the pair of wavelengths needed to retrieve total ozone from runtime namelist file.

O3T_getshp

This subroutine determines the merged *a priori* ozone profile shape given ozone, day and latitude.

O3T_getsur_set

This subroutine reads in a surface category, or land-sea.

O3T_glnchk

This subroutine computes residue at 360nm, logical glint indicator, and glint cloud fraction.

O3T_insurf_set

This subroutine determines the surface category based on the input latitude and longitude.

O3T_iztrsb

This subroutine performs angle and pressure interpolations for one wavelength index and one ozone profile index of the table parameters i_0, T_r , and s_b , which are used by the calling routines to calculate table radiances or N-values. It uses Lagrangian interpolation for angles and pressures except for high clouds for which a linear extrapolation is used.

O3T_lnk_denum

This subroutine calculates product of $(Y_i - Y_k)(Y_i - Y_{k+1}) \dots (Y_i - Y_{i-1})(Y_i - Y_{i+1}) \dots (Y_i - Y_{k+n-1})$ in Lagrange calculation.

O3T_lpoly_cden

This subroutine calculates the coefficients used in Lagrangian interpolation.

O3T_lpoly_coef

This subroutine calculates product of $(Y - Y_k)(Y - Y_{k+1}) \dots (Y - Y_{i-1})(Y - Y_{i+1}) \dots (Y - Y_{k+n-1})$ in Lagrange calculation.

O3T_lpolycden_dispose

This subroutine releases the allocated arrays for Lagrange interpolation.

O3T_lpoly_interp1

This subroutine performs angles (log of 1/COS(angles)) Lagrangian interpolations for one wavelength index, one ozone profile index, and one pressure level index of the table parameters i_0 , T_r , and s_b .

O3T_lpoly_interpPLW

This subroutine performs solar and view angles (Log of 1/COS (angles)) Lagrangian interpolations for all (4) the pressure levels (P), all (12) the layers (L), and the entire wavelength (W) index range from [iwl_s, iwl_e], of the table parameters i_0 , T_r and s_b .

O3T_nvalm

This subroutine computes N-value. The N-value is defined as the negative \log_{10} of the ratio of radiance and irradiance.

O3T_nval_dispose

This subroutine releases the allocated arrays for pre-calculated N-value table.

O3T_nval_setup

This subroutine reads in tables for calculation of forward model quantity: n-value.

O3T_ozfraction

This subroutine calculates the linear interpolation (if input ozone lies between the input lower loading ozone profile iplow) or linear extrapolation (if input ozone lies outside the two profiles iplow and iplow+1) fraction. Note that the ozone amounts are pressure corrected for the profiles.

O3T_oznot

This subroutine computes initial ozone estimate using the 317.5nm wavelength.

O3T_pixgeo_set

This subroutine sets up geo-location information for one particular pixel.

O3T_prof_check

This subroutine performs various profile checks against reference profile, including array size check, negative ozone check, and ratio check in each layer.

O3T_rad

This subroutine performs log linear interpolation or extrapolation for the input parameters of two bracketing ozone profile and produce the normalized radiance.

O3T_resadj

This subroutine adjusts residues after calculation of best ozone.

O3T_residue

This subroutine computes residues for each of the multiply scattered wavelengths.

O3T_step1

This subroutine is the driver program to perform step-one ozone calculation. The algorithm uses a pair of wavelengths by deriving reflectivity from 331 nm and ozone from 318nm. This is an iterative process

which starts with an initial guess ozone, and converges when the reflectivity and the ozone become consistent, meaning that the measured radiances for the pair are equal (within limit) to the calculated radiances based on the reflectivity and the a standard profile of the total ozone loading. The different pair (331&360) may be used under high ozone and high solar zenith angles.

O3T_step2

This subroutine is the driver program for step-two ozone retrieval. It applies ozone and temperature climatologies at all levels to account for seasonal and latitudinal variations in profile shape.

O3T_step3

This subroutine corrects step-two total ozone for wavelength dependence effects, such as tropospheric aerosol, sun glint, and local upper-level profile-shape effects.

O3T_stnprof_1stG

This subroutine determines first guess ozone profile and $\frac{dX}{d\Omega}$.

O3T_stnprof_idxf

This subroutine calculates the profile index based on the input latitude band and the ozone amount. The ozone amount is in between the returned profile index *iplow* and *iplow+1* for most realistic ozone amount in the latitude band.

O3T_stp2oz

This subroutine computes step-two total ozone value.

RD_GOTCO

This function is for reading in HDF formatted GEO files from IDPS output.

RD_SOMTC

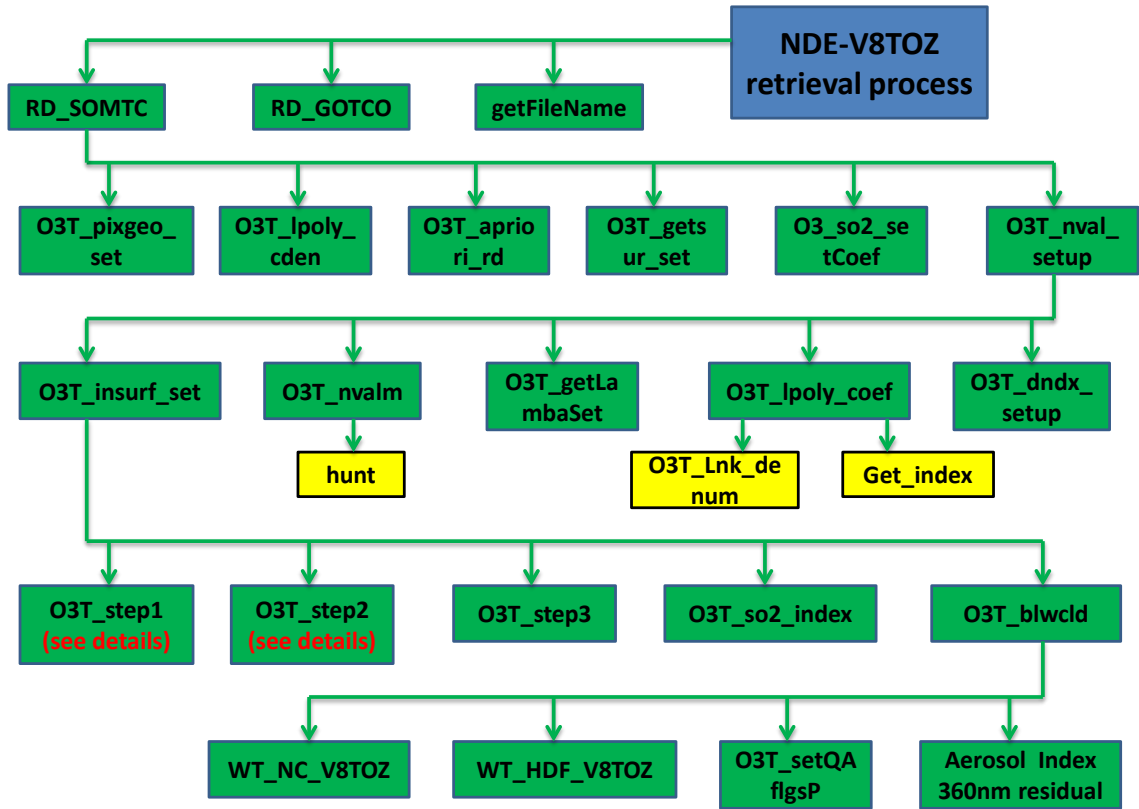
This function is for reading in HDF formatted SDR files from IDPS output.

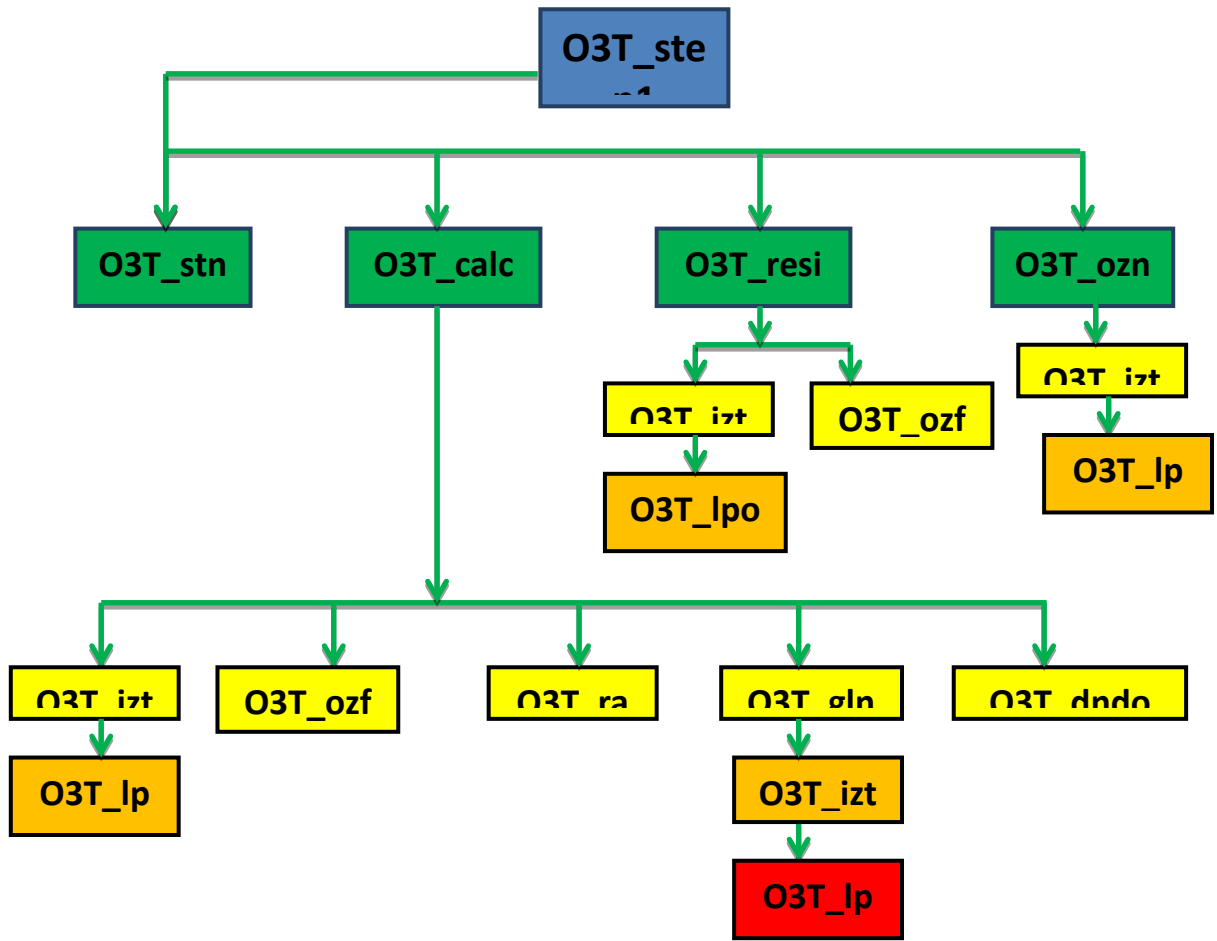
WT_NC_V8TOZ

This function is for writing output in NetCDF files.

WT_HDF_V8TOZ

This function is for writing output in HDF files.





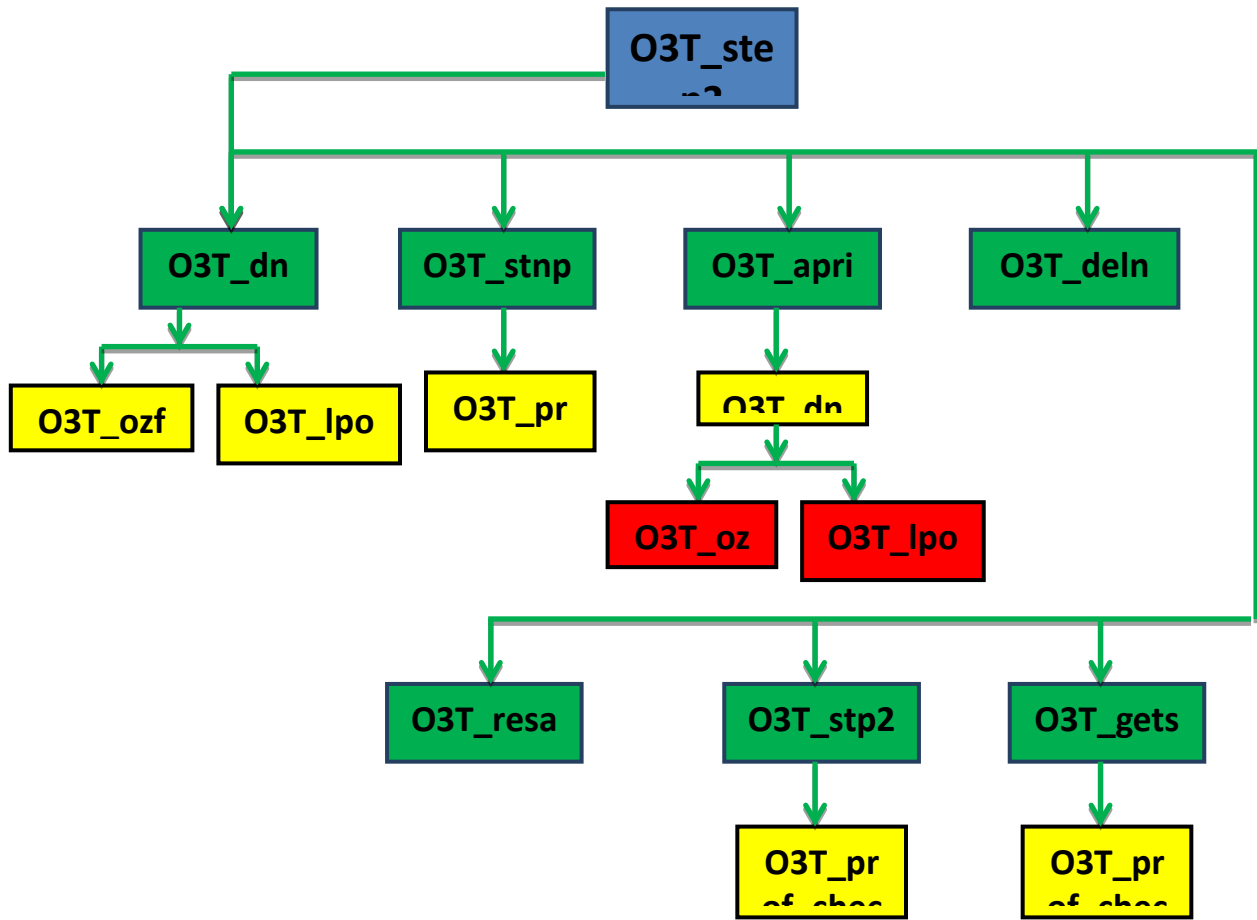


Figure 2-1: These three charts show the program flow for all elements of the OMPS V8TOz.

The modules for NDE-V8TOZ algorithm:

- Climatology_class.f90
- O3T_apriori_class.f90
- O3T_class.f90
- O3T_const.f90
- O3T_dndx_class.f90
- O3T_dndx_m.f90
- O3T_input_class.f90
- O3T_irrad_class.f90
- O3T_iztrsb_m.f90
- O3T_lpolycoef_class.f90
- O3T_lpolyinterp_class.f90
- O3T_nval_class.f90
- O3T_omps.f90
- O3T_output_class.f90

O3T_pixel_class.f90
O3T_radgeo_class.f90
O3T_so2_class.f90
O3T_stnprof_class.f90
UTIL_mmddInterp_class.f90
UTIL_tools_class.f90

2.2. Algorithm Input

Full description of the attributes of all input data used by the algorithm, including primary sensor data, ancillary data, forward models (e.g. radiative transfer models, optical models, or other model that relates sensor observables to geophysical phenomena) and look-up tables. Do not include file formats; these will be documented elsewhere. (*Document Object 14*)

Writers: Algorithm Scientists.

Input Satellite Data

NDEV8T is a system operated within the NDE DHS by OSPO. It uses measurements from the Ozone Mapping and Profiler Suite (OMPS) Nadir Mapper (NM) on the Suomi National Polar-orbiting Partnership (S-NPP) platform and will continue with OMPS on future satellites of the Joint Polar Satellite System (JPSS). S-NPP was launched on October 28, 2011. It is in a sun synchronous orbit with a 1:30pm ascending-node orbit at an altitude of 829 km.

The OMPS NM instrument is a pushbroom spectrometer with a 2-dimensional CCD array detector. The telescope images a 105° cross-track FOV onto the array, providing full daily coverage of the sunlit Earth. It has 196 spectral bands covering the spectrum between 300 nm to 380 nm with 1.1 nm FWHM and 0.42-nm sampling. The instrument is highly flexible and is currently operated to aggregate approximately 20 spatial pixels into 35 cross-track bins and to integrate for approximately 7.8 S. This produces 50x50 km² size products at nadir. Plans for J-01 are to reduce both dimensions by a factor of three and create 103 cross track bins every 2.6 S with 17x17 km² size products at nadir.

The grating spectrometer and focal plane for total column measurements provide 0.42 nm spectral sampling across the wavelength range of 300 to 380 nm. The radiance/irradiance ratios for the 12 wavelengths for the V8TOz EDR algorithm are obtained by interpolating the values at adjacent measurement wavelengths to provide them at the following 12 wavelengths:

[308.7,310.8,311.9,312.61,313.2,314.4, 317.6,322.4,331.3,345.4,360.2,372.8] nm

Satellite Data Preprocessing Overview

The OMPS Raw Data Records (RDRs) are processed at IDPS into Sensor Data Records (SDRs) by the OMPS NM SDR and OMPS NM geolocation algorithms. This processing includes the geolocation and radiometric calibration of the raw sensor output. Details of the OMPS SDR algorithm are described in the JPSS OMPS SDR ATBD.

Input satellite data description

The NDEV8T algorithm uses the radiance and irradiance measurements provide in the OMPS NM SDR and the geolocation and viewing geometry information provided in the OMPS NM GEO. Table 2-1 provides a summary of the OMPS SDR and GEO parameters used by the algorithm.

Table 2-1 OMPS SDR and GEO data used by the NDEV8T algorithm

Input	Type	Description	Units/Valid Range
Pixel-Level Data Items			
satza	real	Satellite zenith angle	Degrees
sza	real	Solar zenith angle	Degrees
xphi	real	Relative azimuth angle between sensor and solar azimuth angles	Degrees
month	integer	Month of measurement	Month / 1 – 12
day	integer	Day of month of measurement	Day
seconds	long integer	Seconds in day of measurement	Seconds
xlat	real	Latitude of measurement	Degrees / -90 – 90
xlong	real	Longitude of measurement	Degrees / -180 – 180
xm	real	Radiances for 24 sensor wavelengths	W/m ² -nm / 0 – 3x10 ⁷
Sflux	real	Solar flux for 24 sensor wavelengths	W/m ² -nm / 0 – 3x10 ⁷

Input Ancillary Data – Climatology and RT LUTs.

The NDEV8T uses climatological values for Cloud Top Pressure, Snow/Ice Fields, Surface Pressure and for Ozone and Temperature Profiles. It also uses radiative transfer Look-Up Tables to provide estimates of the top-of-atmosphere radiance/irradiance ratios (and their sensitivities to ozone layer perturbations) for standard ozone profiles and a select array of viewing conditions. Table 2-2 provides a summary of the climatological and table parameters used by the algorithm.

Table 2-2 Climatological and Table data used by the NDEV8T algorithm

Input	Type	Description	Units/Valid Range
Pixel-Level Data Items			
WI0	real	12 sensor wavelengths to use for measurement	nm / 290 – 390
pcloud	real	Cloud top pressure climatology	hPa / 0 – 1013.25
pteran	real	Terrain pressure climatology	hPa / 0 – 1013.25
prftemp	real	Temperature profile climatology for 11 Umkehr layers	Degrees Kelvin (K) / 170 – 350
isnow	integer	Snow/ice flag	Unitless / 0 – 1
prfoz	real	TOMS V8 Ozone Profile Climatology Data for 11 Umkehr layers	DU / 0 – 999 (0 – 200 for non-fill)
cwavl	real	Wavelength for absorption coefficient	nm / 290 – 390
c0	real	Absorption coefficient at cwavl at 273 K	atm / cm / 0 – 5
c1	real	Linear temperature correction Coefficient to c0	atm / cm / K / 0 - 0.08
c2	real	Quadratic temperature correction Coefficient to c0	atm / cm / K ² / -0.002 to 0.002
o3abs	real	Ozone absorption coefficients used in SOI algorithm	atm / cm /
logi0,z1, z2, tr, knb, sb	real	OMPS V8TOz LUT values	
logi0_dndx, z1_dndx, z2_dndx, tr_dndx, knb_dndx, sb_dndx	real	OMPS V8TOz Sensitivity LUT values	

2.3. Theoretical Description

2.3.1. Physical Description

Comprehensively describe the sensor physics and the associated geophysical phenomenology key to the product retrieval. (*Document Object 15*)

Writers: Algorithm Scientists.

This chapter describes the theoretical basis of the measurements used in the Version 8 algorithms (V8). V8 is the most recent version of the backscattered ultraviolet (BUV) algorithms that have undergone three decades of progressive refinement. Its predecessors, V7 for total ozone, developed about in 1998, and V6 for profile ozone, developed in about 1990, have been used to produce the acclaimed TOMS total ozone and SBUV(2) ozone profile time series. V8 will correct several small errors in V7 and V6 that were discovered by extensive error studies using radiative transfer models and by comparison with ground-based instruments. The V8TOZ uses only two wavelengths (318 nm and 331 nm) to derive total ozone. Other wavelengths are used for diagnostics and error correction. Experience with TOMS and SBUV/2 suggests that the algorithm is capable of producing total ozone with rms error of about 2%, though these errors are not necessarily randomly distributed over the globe. The errors typically increase with solar zenith angle and in presence of heavy aerosol loading.

The OMPS Nadir instruments provide measurements of Earth's total column ozone by measuring the backscattered Earth radiance at a set of discrete 1.1-nm wavelength bands. Both ozone-absorbing and non-absorbing regions of the BUV spectrum are sampled, and the concept of differential absorption is used to derive total column ozone from these measurements. The OMPS-NP uses a double

monochromator to sample the BUV radiation at nadir in 147 discrete wavelength channels from 250 nm to 310 nm. The OMPS uses periodic measurements of the sun to provide normalization of the BUV radiances to solar output, and to remove some instrument dependence. The OMPS instruments measure radiance and irradiance with the same optical system. The OMPS NP instruments cover 14 nadir tracks on the daylight portions of each day's orbits. The OMPS NM instruments also have 14 orbital tracks but their wide angle field-of-view provides daily coverage of the full sunlit globe. The sun synchronous near-polar orbits provide these measurements at the same approximate local time on a monthly basis. Ozone profiles and total column amounts are derived from the ratio of the observed backscattered spectral radiance to the incoming solar spectral irradiance. This ratio is referred to as the backscattered albedo. The only difference in the optical components between the radiance and irradiance observations is the instrument diffuser used to make the solar irradiance measurement; the remaining optical components are identical. Therefore, a change in the diffuser reflectivity will result in an apparent trend in ozone. This is the key calibration component for the OMPS series. The OMPS uses dual sets of diffusers, called the working and reference diffusers, in tandem to monitor the diffuser changes and separate out instrument detector and throughput degradation. The working diffuser is used bi-weekly and the reference diffuser bi-annually. An on-board calibration system using LEDs to illuminate the detector checks for flat fielding and the linearity of the system. A more detailed description of the on-orbit calibration is described in *Seftor et al. 2014*.

This document is organized as follows. The next sections of this chapter provide an overview of key properties of backscattered ultraviolet radiation in the wavelength range used to derive total column and vertical profile ozone, the following chapter describes the theoretical basis of the V8TOZ, including an error analysis, and the third chapter describes the V8PRO.

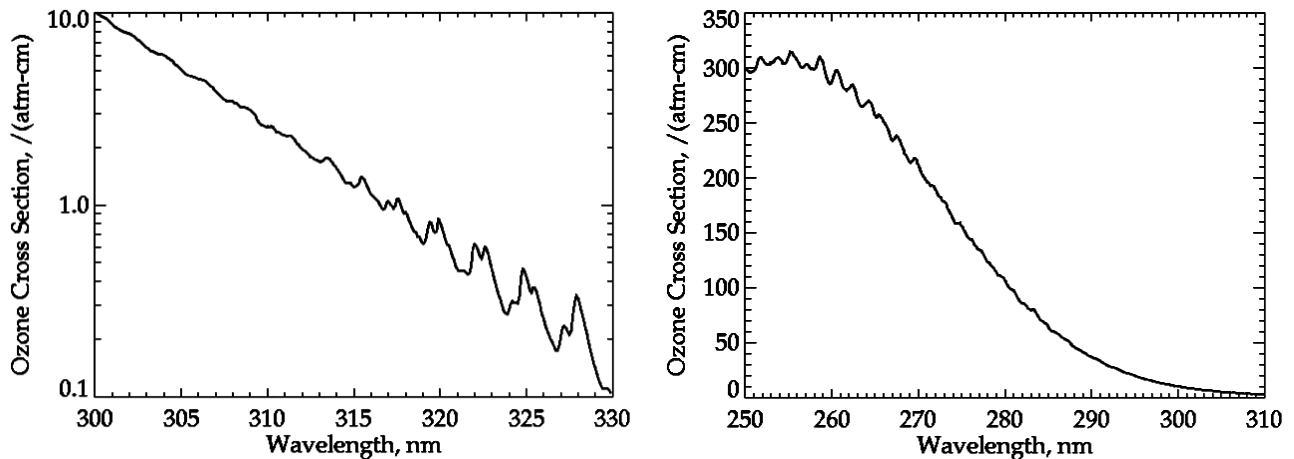


Figure 1-1a (Left) & 1-1b (Right): Ozone Absorption Cross-Sections for 250 nm to 310 nm

1.2 Properties of Backscattered UV (BUV) Radiation
 The OMPS NP and NM instruments together measure the radiation backscattered by the Earth's atmosphere and surface at discrete wavelengths in the range 250 nm to 380 nm. Though ozone has absorption over this entire wavelength range (Fig. 1-1a and Fig 1-1.b), the ozone profile products are retrieved by using wavelengths between 250 nm and 310 nm, where the absorption limits the penetration into the stratosphere; and the total ozone products are derived using UV wavelengths, between 310 nm and 331 nm, where the absorption is significant enough to permit reliable retrievals,

but not so large that they are absorbed before sensing most of the ozone layer. Longer wavelengths are used to identify aerosols and clouds. In the following sub-sections we summarize key properties of the UV radiation in the 250 nm to 380 nm wavelength range that form the basis for the algorithms described in the subsequent chapters.

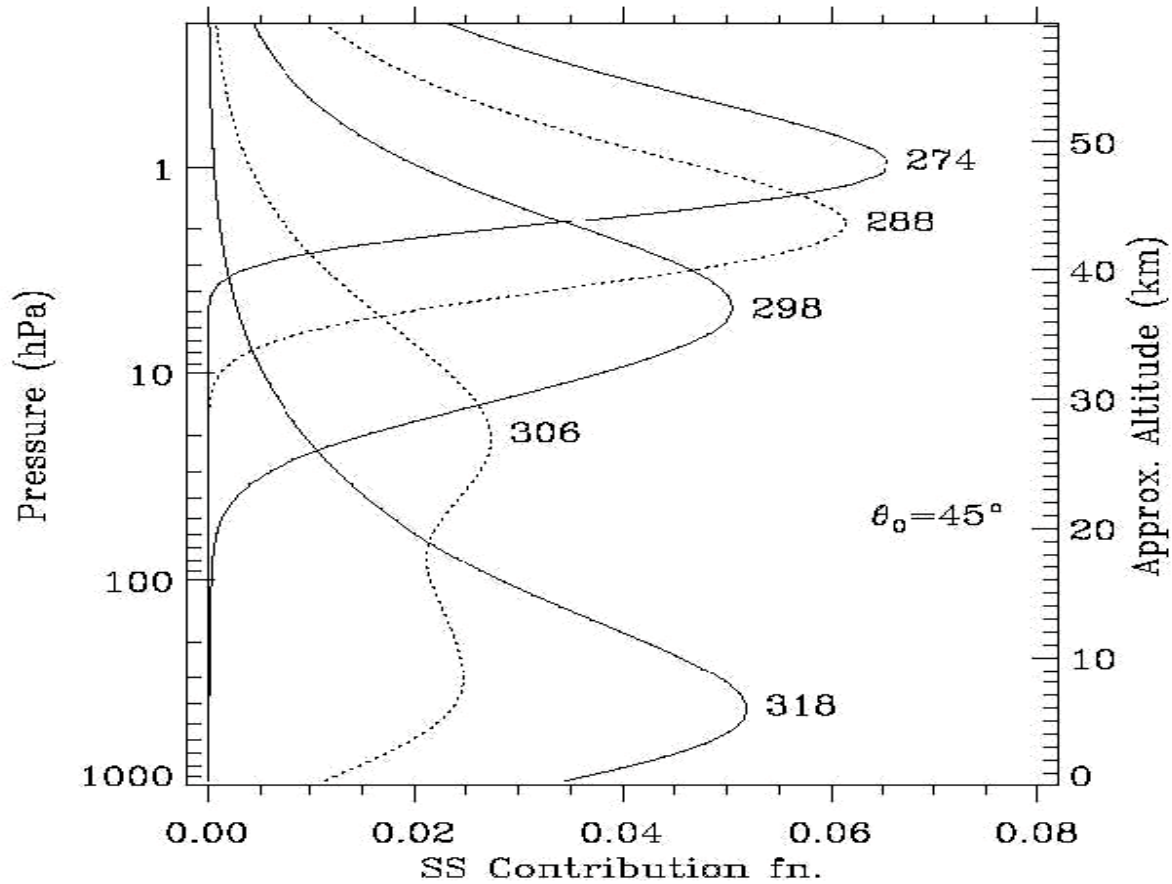


Figure 1-2: Radiance Contribution Functions for selected UV channels

1.2.1 O₃ Absorption

By multiplying the ozone cross-sections given in Fig. 1-1 with typical O₃ column density of 1×10^{19} molecule/cm², one gets the vertical absorption optical depth of the atmosphere, which varies from 160 at 250 nm to 0.01 at 340 nm. Since 90% of this absorption occurs in the stratosphere, little radiation reaches the troposphere at wavelengths shorter than 295 nm, hence the radiation emanating from the Earth at these wavelengths is unaffected by clouds, tropospheric aerosols, and the surface. Therefore, the short wavelength UV radiation consists primarily of Rayleigh-scattered radiation from the molecular atmosphere, with small contributions by scattering from stratospheric aerosols [Torres & Bhartia, 1995], polar stratospheric clouds (PSC) [Torres et al., 1992], polar mesospheric clouds (PMC) [Thomas, 1984]; and emissions from NO [McPeters, 1989], Mg⁺⁺ and other ionized elements. Ozone absorption controls the depth from which the Rayleigh-scattered radiation emanates. As shown in Fig. 1-2, this occurs over a fairly broad region of the atmosphere (roughly 16-km wide at the half maximum point) defined by the radiance contribution functions (RCF). As shown by Bhartia et al. [1996], the

magnitude of the UV radiation is proportional to the pressure at which the contribution function peaks, which occurs roughly at an altitude where the slant ozone absorption optical path is approximately 1. This means that the basic information in UV radiation is on the ozone column density as a function of pressure.

Figure 1-2 also shows that the RCF becomes extremely broad at around 300 nm with two distinct peaks; one in the stratosphere the other in the troposphere. At longer wavelengths the stratospheric peak subsides and the tropospheric peak grows. Since roughly 95% of the ozone column is above the tropospheric peak, the radiation emanating from the troposphere essentially senses the entire ozone column, while the radiation emanating from the stratosphere senses the column above the RCF peak. Thus the longer wavelengths (>310 nm) are suitable for measuring total ozone and the shorter (<310 nm) are suitable for measuring the vertical distribution of ozone profiles. The magnitude of the UV radiation that emanates from the troposphere is determined by molecular, cloud, and aerosol scattering, reflection from the surface, and absorption by aerosol and other trace gases. Basic information about each of these is provided in the following sections.

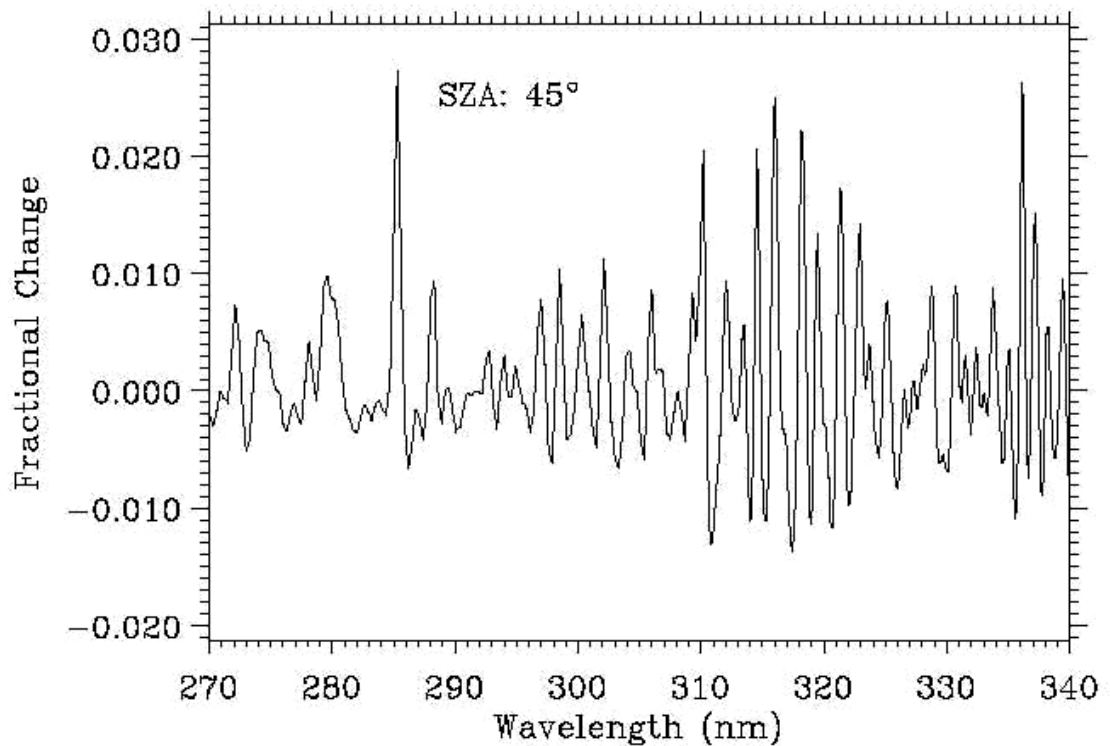


Figure 1-3: Fractional change in UV radiance due to Ring Effect.

1.2.2 Molecular Scattering

In absence of clouds, Rayleigh scattering from the molecular atmosphere forms the dominant component of radiation measured by satellites in the 250 nm to 380 nm wavelength range. Using the standard definition [Young, 1981], we define Rayleigh scattering as consisting of conservative scattering as well as non-conservative scattering, the latter consisting primarily of rotational Raman scattering (RRS) from O₂ and N₂ molecules [Kattawar et al., 1981, Chance et al., 1997]. Though molecular scattering varies smoothly with wavelength, following the well-known $\lambda^{-\alpha}$ law (where α is

approximately 4.3 near 300 nm), RRS, which contributes ~3.5 % to the total scattering, introduces a complex structure in the UV spectrum by filling-in (or depleting) structures in the atmospheric radiation, producing the so-called Ring Effect [Grainger & Ring, 1962] (See Fig. 1-3.). The most prominent structures in UV radiation are those due to solar Fraunhofer lines, however, structures produced by absorption by ozone and other molecules (principally volcanic SO₂) in the earth's atmosphere are also altered by RRS. (Vibrational Raman scattering from water molecules can also produce the Ring effect. Although this effect is insignificant below 340 nm, it can be important at longer wavelengths.) Radiative transfer codes have been developed recently [Joiner et al., 1995; Vountas et al., 1998] that calculate the effect of gaseous absorption, surface reflection and multiple scattering on the Ring signal. These models show that the fractional Ring Effect (*i.e.*, fractional increase or decrease in UV radiation due to RRS) is a complex, non-linear function of surface albedo, aerosol properties, and cloud optical depth, and is also affected by cloud height [Joiner & Bhartia, 1995]. These effects must be accounted for in developing the ozone retrieval algorithms.

1.2.3 Trace Gas Absorption

Besides O₃, SO₂ can produce strong absorption in the 290 nm to 340 nm band. Fig. 1-4 shows that at some wavelengths, a molecule of SO₂ can have four times stronger absorption than a molecule of O₃. However, the background vertical column density (VCD) of SO₂ in the atmosphere is very small (less than 0.1% of ozone), and most of it is in the boundary layer where, because of shielding by molecular scattering, the absorption by a molecule of SO₂ reduces by a factor of 5-10 from that shown in Fig. 1-4. For this reason, even localized enhancements of boundary layer SO₂ due to industrial emission, which can increase VCDs by a factor of 10 or more, are difficult to detect in the UV radiance. However, episodic injection of SO₂ by volcanic eruptions can produce VCDs from 10% of total ozone to more than twice the total ozone [Krueger, 1983; McPeters et al., 1984], thus greatly perturbing the UV radiances.

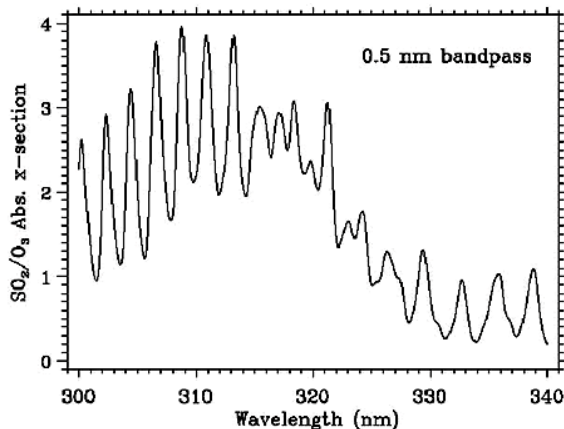


Figure 1-4: Ratio of SO₂ to O₃ absorption cross-section

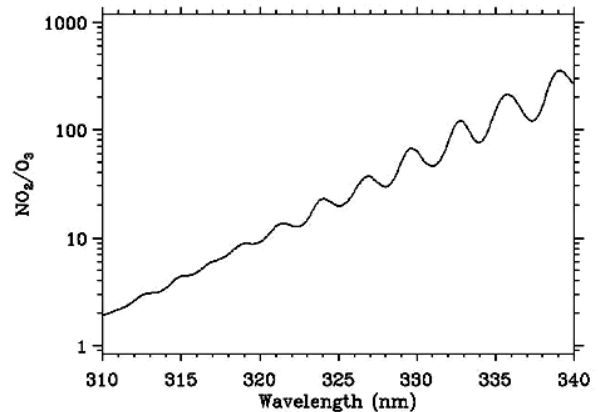


Figure 1-5 Ratio of NO₂ to O₃ absorption cross-section

As shown in Fig. 1-5, on a per molecule basis, NO₂ has much stronger absorption than O₃ at wavelengths longer than 310 nm. However, the VCD of NO₂ in the atmosphere is about 3000 times smaller than O₃, so the NO₂ absorption becomes important only at wavelengths longer than 325 nm, where the NO₂ absorption exceeds 1% of the O₃ absorption. (Like SO₂, boundary layer NO₂ has a 5 to 10 times smaller effect on UV.)

1.2.4 Cloud Scattering

Clouds produce two important effects. Firstly, they alter the spectral dependence of the BUV radiation by adding radiation scattered by cloud particles to the Rayleigh-scattered radiation. Though radiation scattered by clouds is inherently wavelength independent in the UV, the effect of clouds on BUV radiation is strongly wavelength-dependent, depending upon the fraction of the radiation that reaches the cloud altitude. Thus, while tropospheric clouds have no effect on BUV radiation for $\lambda < 295$ nm, PSCs and PMCs do affect those radiances. At longer wavelengths, cloud effects rapidly increase, becoming as large as 60% of the total radiation at 340 nm when deep convective clouds are present. One may think that given the complex geometrical structure of the clouds, and large variations in their microphysical properties, it would be difficult to model the effects of clouds on the BUV radiation. However, TOMS data show (Fig. 1-6.) that the effects of clouds on the spectral dependence of BUV radiation is surprisingly well-defined. Given the low amount of scatter in the data, it appears that both thin clouds that cover the entire scene, as well as broken clouds, which might produce the same 380 nm TOA reflectance, also produce very nearly the same spectral dependence.

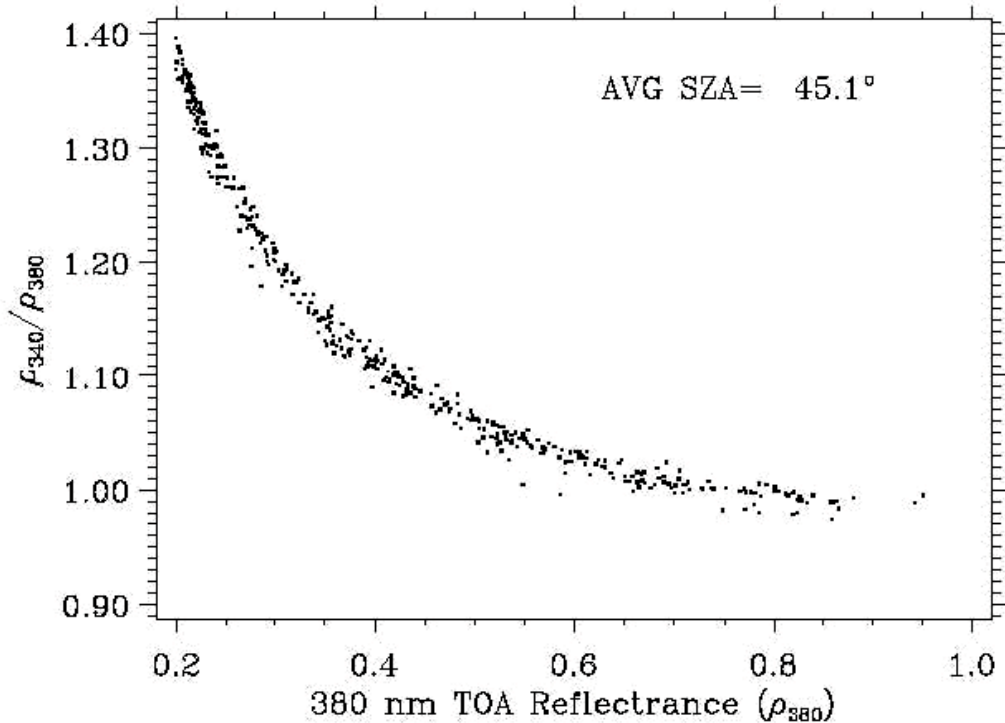


Figure 1-6: Ratio of 340/380 TOA reflectance vs. 380-nm reflectance observed

Similar results from a theoretical study were reported by *Koelemeijer & Stammes [1999]*. This gives the confidence that simple cloud models using TOA reflectance at a weakly absorbing UV wavelength as input may do an adequate job explaining the spectral dependence of TOA reflectance in the UV. A second effect of clouds is that they alter the absorption of BUV radiation by ozone (as well as UV-absorbing aerosols, tropospheric NO_2 , and SO_2 , when they are present). Absorption below the cloud layer is reduced while the absorption inside and above cloud is enhanced. These effects are complex; a function of a cloud's optical thickness, geometrical thickness (which determines the amount of absorbers inside the cloud), and height and the surface albedo, and, of course, wavelength and observation geometry. Fortunately, these effects are usually small, for there is little O_3 or SO_2 in the

troposphere, except in highly polluted conditions. However, thick PSCs and PMCs can introduce large errors [See *Torres et al., 1992; Thomas, 1995*].

1.2.5 Aerosol Scattering

Though the effect of aerosol scattering on UV radiation is usually small compared to the effect of clouds (with the exception of stratospheric aerosols produced after some volcanic eruptions), this effect can be surprisingly complex [*Torres et al., 1998*] depending both on their macrophysical properties (vertical distribution, and optical depth) as well as their microphysical properties (size distribution and refractive index). Figure 1-7 shows how three different aerosol types affect UV radiance at the ozone-absorbing wavelengths. The solid line in Fig. 1-7 represents the case for most common type of aerosols found around the globe. These aerosols contain sea-salt and sulfate and have low levels of soot. Their effect on UV radiance is very similar to that from low level clouds, so they usually require no special consideration. However, aerosols that absorb UV radiation, *e.g.*, continental aerosols containing soot (dotted line), carbonaceous aerosols (smoke) produced by biomass burning (not shown), and mineral dust (dashed line) from deserts reduce the UV radiation passing through them, so they cause the underlying surface (including clouds) to appear darker. If a layer of UV-absorbing aerosols is above a dark surface, the amount of radiation they absorb is strongly dependent on the layer altitude, the higher the aerosol the larger the effect. Sometimes, it is assumed that the effect of aerosols on UV radiation is a simple linear (or quadratic) function of wavelength. As shown in Fig. 1-7, this assumption is not valid at wavelengths below 310 nm; even at longer wavelengths, a layer of thick aerosols can modify trace gas absorption, just like clouds, *i.e.*, the gaseous absorption above and inside the aerosol layer is enhanced while the absorption below the layer is reduced. This effect must be taken into account for accurate retrievals in highly polluted conditions.

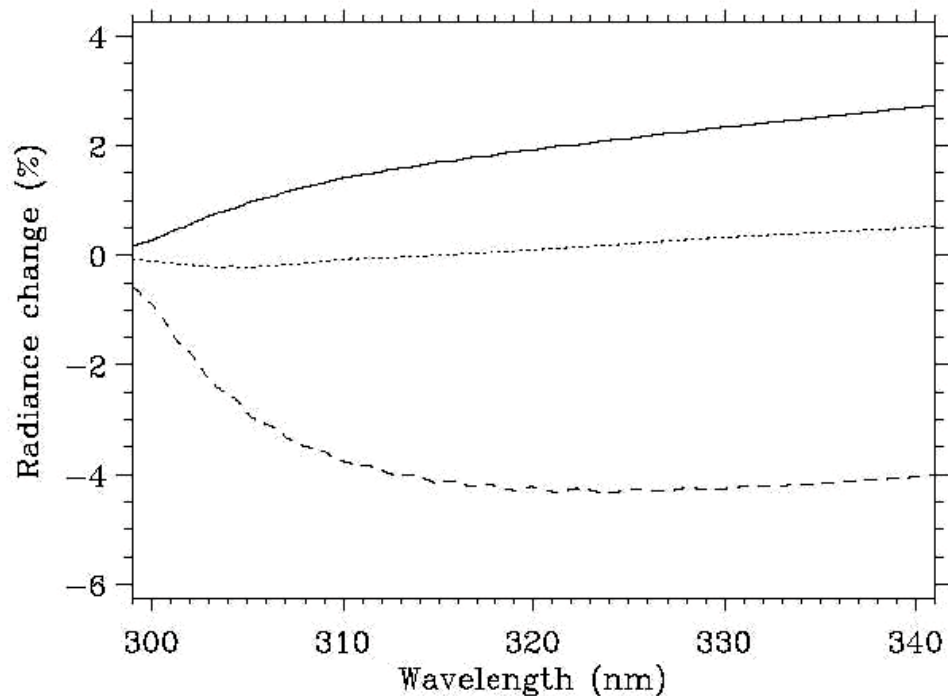


Figure 1-7: Effect of aerosols on UV radiances. (25° solar ZA, nadir view, 0.15

A notable exception is stratospheric aerosols produced after high altitude volcanic eruptions. Stratospheric aerosols of relatively small optical thickness ($\tau \sim 0.1$) can markedly alter the ozone absorption of the BUV radiation [Bhartia et al., 1993, Torres & Bhartia, 1995; Torres et al., 1995], increasing the absorption at some wavelengths, decreasing it at other wavelengths. One needs accurate knowledge of the aerosol vertical distribution to account for these effects.

1.2.6 Surface Reflection

The reflectivity of the Earth's surface in UV is usually quite small [Eck et al., 1987; Herman & Celarier, 1997]. Even over deserts, where the visible reflectivity can be quite high, the UV reflectivity remains below 10%. It exceeds 10% only in presence of sea-glint, snow and ice. More importantly, to the best of our knowledge, the UV reflectivity doesn't vary with wavelength significantly enough to alter the spectral dependence of the BUV radiation. An important exception is the sea-glint. Since the reflectivity of the ocean, when viewed in the glint (geometrical reflection) direction, is very different for direct and diffuse light (exceeding 100% for direct when the ocean is calm, but only 5% for diffuse), in the UV, where the ratio of diffuse to direct radiation has a strong spectral dependence, the ocean appears "red", *i.e.*, it gets brighter as the wavelength increases. The reflectivity of the ocean at any wavelength, as well as its spectral dependence, is a strong function of wind speed, and of course, aerosol and cloud amount. Accurate retrieval in presence of sea glint requires that one account for these complex effects. Fortunately, the nadir-viewing geometry of the OMPS NP and the spacecraft orbits with equator crossing times more than an hour from solar noon limit the occurrence of sea-glint observing geometries. For the OMPS NM, the problematic geometries are identified and flagged if they occur over regions identified as water surfaces.

2.3.2. Mathematical Description

The Version 8 total O₃ algorithm (V8TOZ) is the most recent version of a series of BUV (backscattered ultraviolet) total O₃ algorithms that have been developed since the original algorithm proposed by Dave & Mateer [1967], which was used to process Nimbus-4 BUV data [Mateer et al., 1971]. These algorithms have been progressively refined [Klenk et al., 1982; McPeters et al., 1996; Wellemeyer et al., 1997] with better understanding of UV radiation transfer, internal consistency checks, and comparison with ground-based instruments. However, all algorithm versions have made two key assumptions about the nature of the BUV radiation that have largely remained unchanged over all these years. Firstly, we assume that the BUV radiances at wavelengths greater than 310 nm are primarily a function of total O₃ amount, with only a weak dependence on O₃ profile that can be accounted for using a set of standard profiles. Secondly, we assume that a relatively simple radiative transfer model that treats clouds, aerosols, and surfaces as Lambertian reflectors can account for most of the spectral dependence of BUV radiation, though corrections are required to handle special situations. The recent algorithm versions have incorporated procedures for identifying these special situations, and apply semi-empirical corrections, based on accurate radiative transfer models, to minimize the errors that occur in these situations. In the following sections, we will describe the forward model used to calculate the top-of-the-atmosphere (TOA) reflectances, the inverse model used to derive total O₃ from the measured reflectances, and give a summary of errors.

2.2 Forward Model

The radiative transfer forward model, called TOMRAD, used in creating look-up tables and conducting sensitivity tests is based on successive iteration of the auxiliary equation in the

theory of radiative transfer developed by *Dave* [1964]. This elegant solution accounts for all orders of scattering, as well as the effects of polarization, by considering the full Stokes vector in obtaining the solution. Though the solution is limited to Rayleigh scattering and can only handle reflection by Lambertian surfaces, the original Dave code, written more than three decades ago, is still one of the fastest radiative transfer codes that is currently available to solve such problems, and, with the modifications that have been incorporated into the code over the years, it is also one of the most accurate. The modifications include a pseudo-spherical correction (in which the incoming and the outgoing radiation is corrected for changing solar and satellite zenith angle due to Earth's sphericity but the multiple scattering takes place in plane parallel atmosphere), molecular anisotropy [Ahmad & Bhartia, 1995], and rotational Raman scattering [Joiner et al., 1995]. Comparison with a full-spherical code indicates that the pseudo-spherical correction is accurate to 88° solar zenith angle [Caudill et al., 1997]. The current version of the code can handle multiple molecular absorbers, and accounts for the effect of atmospheric temperature on molecular absorption and of Earth's gravity on the Rayleigh optical depth. In the following we describe the various inputs and outputs of this code.

2.2.1 Spectroscopic Constants

The Rayleigh scattering cross-sections and molecular anisotropy factor used are based on *Bates* [1984], while the O_3 cross-sections and their temperature coefficients are based on *Bass & Paur* [1984] for wavelengths shortward of 340 nm and *Voight et al.* [1998] for 340 nm and longer. The possibility of switching to a new set of O_3 cross-sections based on the laboratory work of *Brion et al.* [1993] is under investigation. The forward model also accounts for O_2 - O_2 absorption, which is based on measurements by *Greenblatt et al.* [1990].

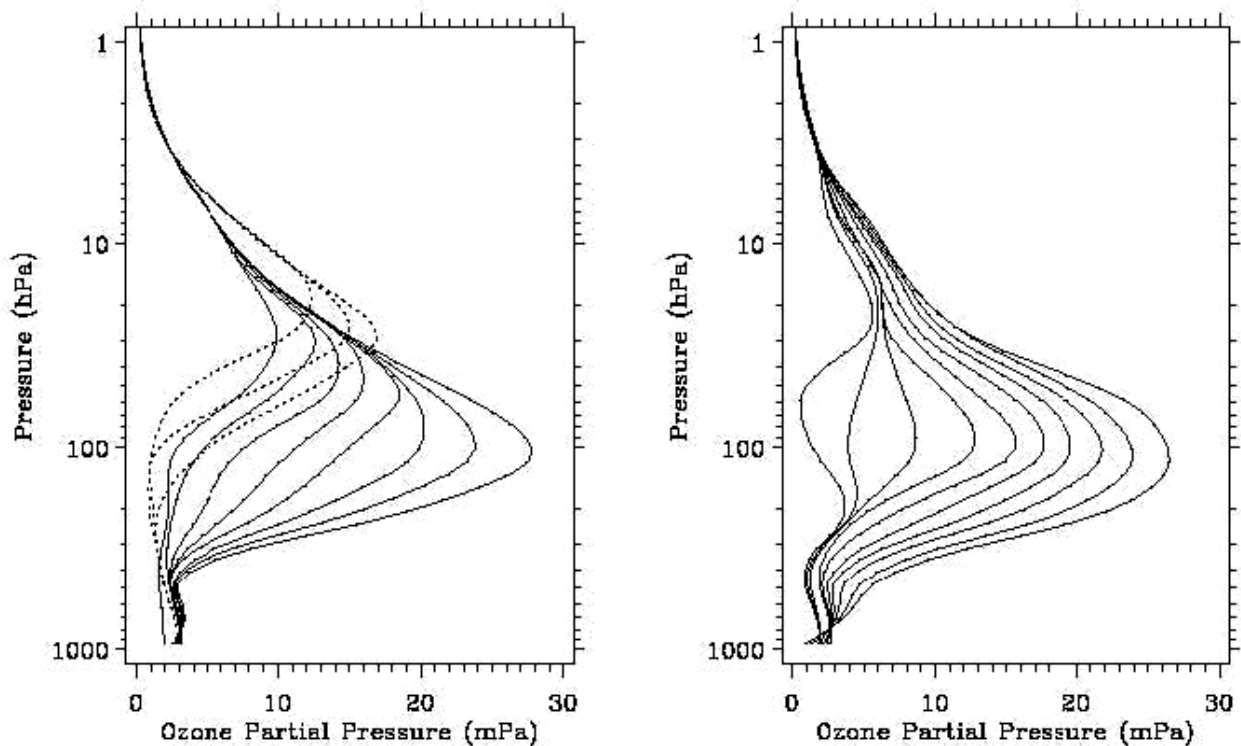


Figure 2-1: Total O₃-dependent standard profiles used for generating the radiance table. The Left panel shows 3 low latitude profiles (dotted lines) and 8 mid latitude profiles. The Right panel shows the 10 high latitude profiles.

2.2.2. O₃ and Temperature Profiles

In general, the UV radiation at any wavelength is a function of O₃ and temperature profiles. Though at 317.5 nm, which is used to derive total O₃ in the V8TOZ algorithm, these effects are usually quite small, they must be accounted for if high accuracy in deriving total O₃ is required. Empirical orthogonal analysis of the ozonesonde data [Wellemeyer et al., 1997] shows that the largest variation in O₃ profiles occurs in the lower stratosphere (10-20 km), and that these variations are highly correlated with total O₃. By contrast, the tropospheric (0-10 km) and upper stratospheric (20-40 km) O₃ density amounts show weak correlation with total O₃, but vary with season and latitude. Recognizing this, the V8TOZ algorithm uses a 3-dimensional dataset of O₃ profiles to compute total O₃, consisting of profiles that vary with total O₃, latitude and month. These profiles are constructed by combining two 2-dimensional datasets described below. The first dataset consists of 21 O₃ profiles (called standard profiles) that vary with total O₃ and latitude. These profiles have been generated by using ozonesonde data below 25 km and SAGE satellite data above. These data are first integrated to obtain O₃ amounts in ten layers (approximately 4.8-km thick), equally spaced in log-pressure with spacing of log(2), extending from 1 atm. (1013.25 hPa) to 2⁻¹⁰ atm. (This smoothes out any high resolution structures that might occur when there are not enough data points to average.) A top layer that extends to infinity is then added by linear extrapolation of a fit of the logarithm of the O₃ amounts in the upper two layers with log-pressure (which is equivalent to assuming that the ratio of O₃ to atmospheric scale height in the top layers is constant). The layer O₃ values are binned two-dimensionally, in 50 DU total O₃ bins, and 30° latitude bins, with data from both hemispheres combined, to provide three profiles for low latitudes (30S-30N) containing 225 DU to 325 DU, eight for mid latitude (30-60) containing 225 DU to 575 DU, and ten for high latitude (60-pole) containing 125 DU to 575 DU. The O₃ partial pressure profiles reconstructed from the layer O₃ amounts are shown in Fig. 2-1. They capture the well-known features of the O₃ vertical distribution, namely, that in a given latitude band the O₃ peak and the O₃ tropopause get lower as total O₃ increases, and for a given total O₃ the peak gets lower as one moves to higher latitude. Empirical orthogonal function analysis shows that the standard profiles capture the first two eigen-functions of the O₃ profile covariance matrix well, and explain about 80% of the variance of the layer O₃ amounts [Wellemeyer et al., 1997]. However, the scheme doesn't capture the seasonal variation of O₃ at altitudes where the O₃ profile is not correlated with total O₃ (the troposphere and altitudes above 25 km). Also, since a single US standard temperature profile is used in constructing the radiance tables, the effects of seasonal and latitudinal variation of temperature on O₃ cross-sections are not accounted for. The previous UV algorithms had ignored these effects, since their absence did not increase the RMS error of a single measurement significantly and had virtually no impact on global O₃ trend. This practice is consistent with that used by ground-based Dobson instruments, which also ignore seasonal and latitudinal variations in atmospheric temperature in retrieving total O₃ from their measurements. However, with improving accuracy of the various O₃ measuring systems, and with increasing emphasis on extracting weak tropospheric O₃ signatures from total O₃ measurements [Fishman et al., 1986; Ziemke et al., 1998] these small errors become more noticeable. We correct these errors in V8TOZ by

incorporating monthly and latitudinally varying O₃ and temperature climatologies in the retrieval algorithm [based on the work described in *McPeters, Logan, & Labow 2003*].

The 3-dimensional profiles are constructed by combining these two datasets in such a way that in the part of the atmosphere where total O₃ is a good predictor of O₃ profile the 1st dataset prevails while in the rest of the atmosphere the 2nd data set prevails. This results in 1512 profiles, 12Xn profiles in each of the 18 latitude bins, where n is 3 in low latitudes (30S-30N), 8 in mid latitude (30°-60°), and 10 in high latitudes (60°-90°), containing the same total O₃ as in the first dataset. These profiles are slightly different in the two hemispheres, primarily due to hemispherical asymmetry in the tropospheric O₃. Since the errors in switching from the 21 profiles to the larger set are small, we have judged that it is sufficiently accurate to correct for them using Jacobians - defined as $d\log I/dx$, where I is the TOA (top of atmosphere) radiance, and x is the layer O₃ amount in ~4.8 km [$\Delta\log(p)=\log(2)$] atmospheric layers. The Jacobian is calculated by the finite difference method for each entry in the basic radiance table. (The Jacobian can be provided in the output file so a user can readily calculate the impact of using an alternative O₃ or temperature profile on the retrieved O₃ without going through the full algorithm. This should be particularly useful for the assimilation of total O₃ data using techniques based on 3-dimensional chemical and transport models.)

Figure 2-2 shows scatter plots comparing layer O₃ amounts measured by the Hohenpeissenberg ozonesonde station with the 96 profile subset of the 3D profiles at that latitude. In layers 2 to 4, the correlations between the two are ~85%. Table 2-1 shows the variation reduction and residual standard deviation with this station and the SAGE satellite data at 50°N. The residual standard deviation in all layers is less than 10 DU. Similar results are obtained at other latitudes.

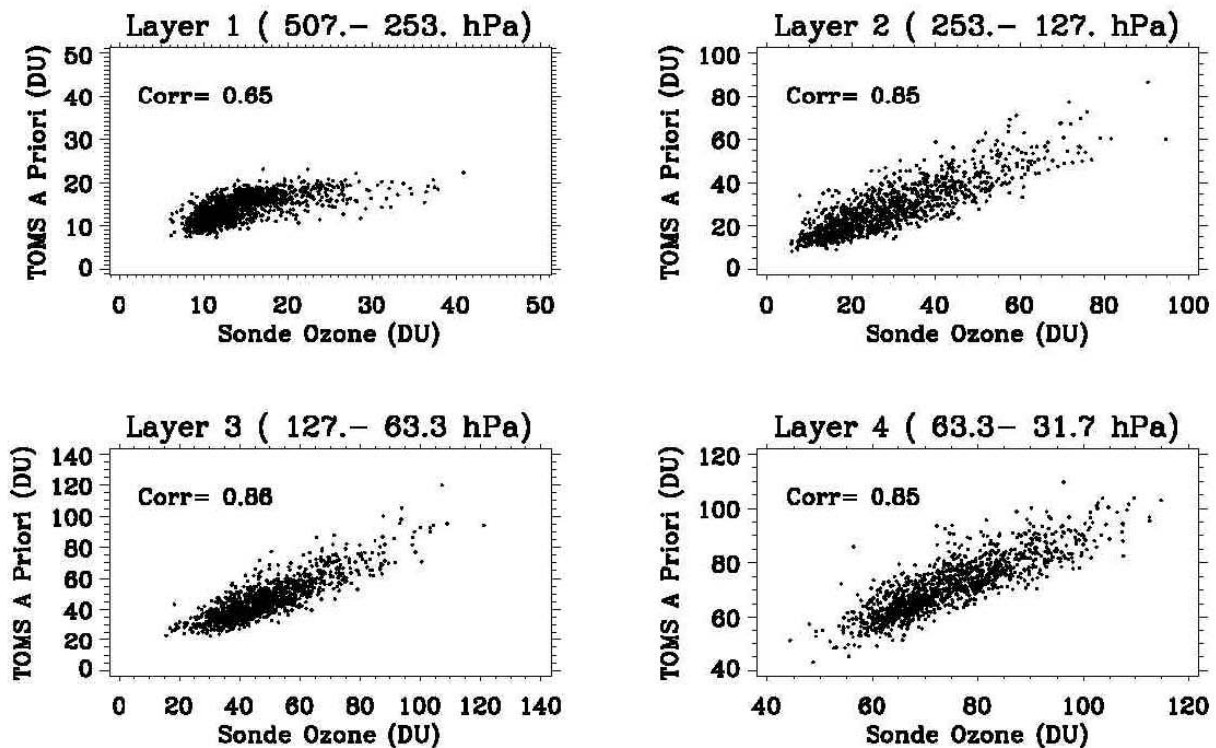


Figure 2-2: Comparisons between Hohenpeissenberg ozonesonde layer amounts and the 96 standard profiles in the 3-dimensional set used at its latitude.

Table 2-1: Comparison of A Priori profiles with ozonesonde and SAGE

Layer (No.)	Layer midpoint (~km)	Hohenpeissenberg		SAGE @50°N	
		Variance reduction (%)	Residual std dev (DU)	Variance reduction (%)	Residual std dev (DU)
0	2.8	41	2.9	-	-
1	7.7	42	3.8	-	-
2	12.5	73	7.6	75	9.7
3	17.0	74	7.4	83	8.9
4	21.3	73	6.0	77	6.4
5	25.8	24	5.5	29	5.3
6	30.4	42	3.5	35	4.3
7	35.2	-	-	39	1.9
8	40.2	-	-	28	1.0
9	45.5	-	-	40	0.5

2.2.3 Surface and cloud pressure

To compute radiances, one needs both the surface pressure and the effective cloud pressure (defined as the pressure from which the cloud-scattered radiation appears to emanate). Surface pressure is obtained by converting a standard terrain height data base using US standard temperature profiles. The cloud top height climatology has been produced by using the coincident measurements of TOMS and the Temperature Humidity Infrared Radiometer (THIR) both onboard the Nimbus 7 Spacecraft. THIR cloud heights for clouds with high UV-reflectivity based on TOMS have been mapped onto a 2.5° latitude X 2.5° longitude grid for each month. These high reflectivity cloud heights are appropriate for the V8TOZ cloud and surface reflectivity model described below in Section 2.2.4. The surfaces are also flagged as containing snow/ice by using a climatological database. There is no difficulty in substituting improved information on ground cover from current observations or forecasts.

2.2.4 Radiance Computation

Using the output of TOMRAD, one calculates the TOA radiance, I , by using the following formula:

$$I = I_0(\theta_0, \theta) + I_1(\theta_0, \theta)\cos\phi + I_2(\theta_0, \theta)\cos 2\phi + \frac{RI_R(\theta_0, \theta)}{(1 - RS_b)} \quad (2.1)$$

where, the first three terms constitute the purely atmospheric component of the radiance, unaffected by the surface. This component, which we will refer to as I_a , is a function of solar zenith angle θ_0 , satellite zenith angle θ , and ϕ , the relative azimuth angle between the plane containing the sun and local nadir at the viewing location and the plane containing the satellite and local nadir. The last term provides the surface contribution, where, the product RI_R is the once-reflected radiance from a Lambertian surface of reflectivity R , and the factor $(1 - RS_b)^{-1}$ accounts for multiple reflections between the surface and the overlying atmosphere. Note that this factor can greatly enhance the effect of absorbers (*e.g.*,

tropospheric O₃, O₂-O₂, UV-absorbing aerosols, and SO₂) that may be present just above a bright surface. The tables are computed for ten solar zenith angles and six satellite zenith angles, which have been selected so that the interpolation errors in the computed radiances are typically smaller than 0.1% using a carefully constructed piecewise cubic interpolation scheme.

The forward model does not account for aerosols explicitly. This decision has been made deliberately since, as shown by *Dave* [1978], common types of aerosols (sea-salt, sulfates etc.) can be treated simply by increasing the apparent reflectivity of the surface, *i.e.*, by increasing R in Eq. (2.1), to match the measured radiances at a weakly ozone-absorbing wavelength. This also avoids the need for knowing the true reflectivity of the surface. However, one must make a key assumption that the reflectivity thus derived is spectrally invariant over the range of wavelength of interest (310 nm to 330 nm). It is now known that UV-absorbing aerosols (smoke, mineral dust, volcanic ash) introduce a spurious spectral dependence in R , for they absorb the (strongly wavelength-dependent) Rayleigh-scattered radiation passing through them [Torres et al., 1998]. This absorption obviously varies with the height of the aerosols as well as on their microphysical properties; both of which are highly variable in space and time. Therefore, it is not possible to account for them explicitly in the forward model. In the next section we will discuss how we detect and correct for them in the inverse model.

The forward model treats a cloud as an opaque Lambertian surface. Transmission through and around clouds is accounted for by a partial cloud model, in which the TOA radiance I is written as:

$$I = I_s(R_s, p_s)(1 - f_c) + I_c(R_c, p_c)f_c \quad (2.2)$$

where, I_s represents radiance from the clear portion of the scene, containing a Lambertian surface of reflectivity R_s at pressure p_s ; and I_c similarly represents the cloudy portion, and f_c is the cloud fraction. As shown in Fig. 2-3, the best agreement between the spectral dependence of TOA reflectance ($\rho = \pi I / F \cos \theta_0$) observed by TOMS and that calculated by using Eq. (2.2) is obtained by setting R_c to 0.80. However, since typical clouds have an albedo of ~ 0.40 , f_c should be viewed as a radiative (effective) cloud fraction, rather than the geometric cloud fraction.

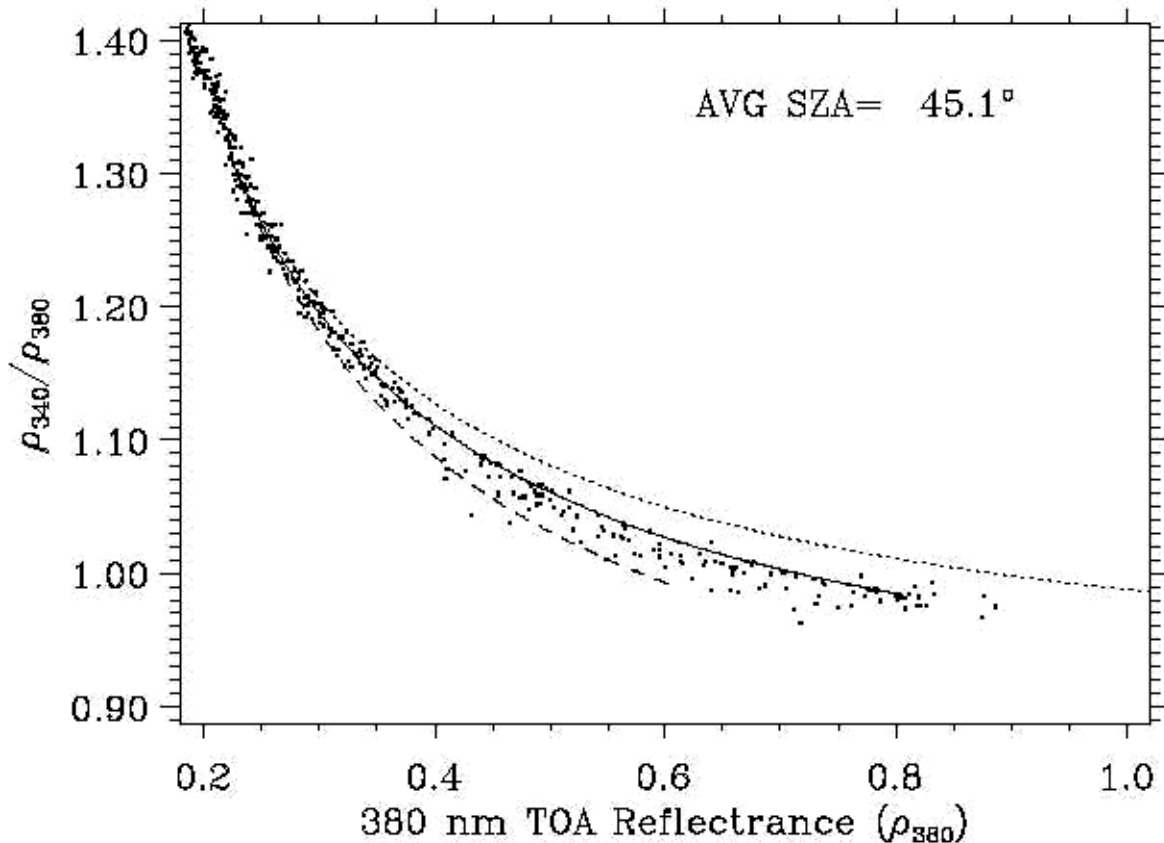


Figure 2-3: Ratio of 340/380 TOA reflectance compared with partial cloud

2.3 Inverse Algorithm

The inverse algorithm consists of a 3-step retrieval procedure. In the first step, a good first estimate of effective reflectivity (or effective cloud fraction) and total O₃ is made by using the 21 standard profile radiance tables and the measured radiance to irradiance ratios at 318 nm and 331 nm. In step 2, this estimate is corrected by using the Jacobians and seasonally and latitudinally varying O₃ and temperature climatology. These corrections typically change total O₃ by less than 2%. In the final step, scenes containing large amounts of aerosols, sea glint, volcanic SO₂, or with unusual O₃ profiles are detected by using an approach based on the analysis of residuals (differences between measured and computed radiances at wavelengths not used in the first two steps). We use pre-computed regression coefficients applied to these residuals to correct for these effects. These coefficients are generated by off-line analysis of the relationship between retrieval errors and residues computed by accurately modeling radiances for a representative set of interfering species/events. An important benefit of this approach is that unusual events are easily flagged so they can be identified later for careful analysis. Past analyses of such events led to the discovery of a new method of studying aerosols by using BUV radiances.

2.3.1 Step 1: Initial total O₃ estimation

This step consists of the following sub-steps.

Step 1.1: By assuming a nominal total O₃ amount, calculate the effective reflectivity of the scene by inverting Eq. (2.1). The inverse equation is:

$$R = \frac{(I_m - I_a)}{[I_R - S_b(I_m - I_a)]} \quad (2.3)$$

where, I_m is the measured radiance at 331 nm, and I_a and I_R are calculated using the climatological surface pressure (p_s) appropriate for the scene. If $0.15 < R < 0.80$, and the snow/ice and sea-glint flags are not set, compute effective cloud fraction f_c by inverting Eq. (2.2), *i.e.*,

$$f_c = (I_m - I_s) / (I_c - I_s) \quad (2.4)$$

where I_s and I_c are computed using Eq. (2.1) assuming $R_s = 0.15$ and $R_c = 0.8$. Note that the surface is assumed to have a reflectivity of 15%, even though the UV reflectivity of most surfaces (not covered with snow/ice) is between 2-8% [Herman & Celarier, 1997]. A larger value is used to account for haze, aerosols, and fair-weather cumulus clouds that are frequently present over the oceans at very low altitudes. We believe that treating them as part of the surface rather than as part of (a higher-level) cloud offers the best strategy to minimize errors. However, the method may produce small errors (1-2 DU) when cirrus clouds are present.

If R derived from Eq. (2.3) is greater than 0.80, we assume that the surface contribution to the radiance is zero. The (Lambertian-equivalent) cloud reflectivity is then derived using Eq. (2.3) assuming the surface is at p_c . When the snow/ice flag is set, we currently assume that the cloud contribution to the radiances is negligible, and that R derived from Eq. (2.3) using p_s represents the surface reflectivity.

Step 1.2: Using R or f_c and equations (2.1) and (2.2) compute the radiance as a function of total O₃ amount (Ω) at 317.5 nm. Estimate O₃ by a piecewise-linear fit on $\log(I)$ vs. Ω , *i.e.*,

$$\Omega_1 = \Omega_i + (\ln I_m - \ln I_i) \left/ \frac{\partial \ln I}{\partial \Omega} \right|_{i,i+1} \quad (2.4)$$

where, the measured radiance I_m lies between I_i and I_{i+1} , computed using profiles with total O₃ amounts Ω_i and Ω_{i+1} , respectively. Iterate steps 1.1 and 1.2 to correct for the total O₃ dependence of the 331.2 nm wavelength. Convergence is achieved in one or two iterations.

At the termination of the iteration, one has the estimated O₃ value Ω_1 , as well as the O₃ profile (\mathbf{X}_1) which has been used to estimate it. This O₃ profile is given by interpolation of the standard profiles, namely,

$$\mathbf{X}_1 = \mathbf{X}_i + (\mathbf{X}_{i+1} - \mathbf{X}_i) (\Omega_1 - \Omega_i) / (\Omega_{i+1} - \Omega_i) \quad (2.5)$$

Where \mathbf{X}_i and Ω_i are ozone profiles and total ozone amounts, respectively, for profile standard profile i .

2.3.2 Step 2: O₃ and Temperature climatology correction

In step 2, we adjust the solution total O₃ to be consistent with a climatological O₃ profile (**X**₂) and a climatological temperature profile (**T**₂). The Step 2 total O₃, Ω_2 is obtained as follows:

$$\Omega_2 = \Omega_1 + \frac{\sum_l [x_{2,l} - x_{1,l}] \frac{\partial \ln I}{\partial x_l} + [\sigma(T_{2,l}) - \sigma(T_{1,l})] \frac{\partial \ln I}{\partial \sigma_l}}{\frac{\partial \ln I}{\partial \Omega}} \quad (2.6)$$

where, l refers to the layer number, and $\sigma(T)$ is the O₃ absorption cross-section at temperature T . The Jacobian $\partial \ln I / \partial \sigma$ is calculated from $\partial \ln I / \partial x$ by using the chain rule for partial derivatives and that the radiances are functions of the products of x and σ , so

$$\frac{\partial \ln I}{\partial \sigma_l} = \frac{\partial \ln I}{\partial x_l} \frac{x_l}{\sigma_l} \quad (2.7)$$

The O₃ profile climatology used to provide (**X**₂) is dependent on latitude and season as well as total O₃. A two step process was used to create the climatology in order to combine available information. First, the total O₃ dependent standard profiles used to produce **X**₁ (Equation 2.5) are combined with a climatology of seasonally and latitudinally varying O₃ profiles that has no total O₃ dependence. This procedure of merging the two climatologies has been carefully designed to account for the strengths and weaknesses of the two. We assume that the total O₃ dependent standard profiles are most accurate in atmospheric layers where the layer O₃ is highly correlated with total O₃ (30 hPa- tropopause), while the seasonal climatology is better in all other layers. The merged climatology of profiles (**X**₂) is constructed as follows:

$$\mathbf{X}_2 = \mathbf{X}_1 + [\mathbf{X}_c - \mathbf{X}_s(\Omega_c)] \quad (2.8)$$

where, **X**_c is the climatological profile (interpolated to the time and location of the measurement) and **X**_s is the standard profile (Fig. 2-1) interpolated to the same total O₃ (Ω_c) as contained in **X**_c. Note that, since Ω_c and Ω_s are the same, the procedure conserves total O₃, *i.e.*, $\Omega_2 = \Omega_1$. It also retains **X**₁ in those layers in which **X**_c and **X**_s are nearly the same. This occurs in those layers where total O₃ is a good predictor of the O₃ profile. In layers in which **X**_s doesn't vary with total O₃ (Fig. 2-1), **X**₁ and **X**_s are the same, so **X**₂ becomes equal to **X**_c.

This procedure works quite well except at high latitudes where the large dynamic range of total O₃ amounts seems to thwart the use of Eq. (2.8) to determine profile shape characteristics for all total O₃ amounts based on a mean profile. In these regions as a second step, we have used SBUV profile information to adjust the total O₃ dependence of the merged climatology.

Comparison with sonde and satellite data shows that the **X**₂ profile set explains a large portion of the variance of the O₃ profiles seen at all altitudes, indicating that Eq. (2.8) provides a reliable method of generating *a priori* O₃ profiles over the entire globe that vary correctly with season and total O₃. The temperature profile **T**₂ corresponding to **X**₂ is obtained simply by interpolation using a (month x latitude) climatology of temperature profiles obtained from NOAA/NCEP data.

2.3.3 Step 3: Correction of errors due to episodic events

Using R (or f_c), which is assumed to be wavelength independent, Ω_2 , and the associated

O₃ and temperature profiles \mathbf{X}_2 and \mathbf{T}_2 , it is straightforward to use the radiance and Jacobian tables to predict the radiance at each OMPS wavelength. We call the percentage difference between the measured and predicted radiances the residuals. If the quantities that have been derived, and the assumptions made in deriving them are valid, the residuals should be zero, so a non-zero residue is an indicator of combined errors due to the forward model, the inverse model and the instrument calibration. Experience with TOMS, supported by extensive simulation of various errors by using radiative transfer code, suggests that the analysis of spatial and temporal variability of the residual can yield many valuable clues to separate these various error sources. In many cases a simple correction procedure based on these residues can be developed. In the following, we provide examples of errors that can be detected and corrected this way.

Aerosols

TOMS data show very clearly that the apparent reflectivity of the Earth's surface derived from Eq. (2.3) has a strong wavelength dependence in the presence of mineral dust and carbonaceous aerosols. Mie scattering calculations show that this is caused by the absorption of direct and Rayleigh-scattered radiation as it passes through the aerosol layer. Since this scattering increases with decreasing wavelength, the apparent reflectivity of the surface (obtained by neglecting the aerosol absorption) decreases with wavelength. When one uses only two wavelengths to derive O₃, this absorption produces an effect that cannot be distinguished from O₃ absorption, and hence one overestimates total O₃. The V8TOZ algorithm corrects for this effect by taking advantage of the fact that the effect on radiances of the R- λ dependence produced by aerosols can be readily observed by using two weakly-absorbing wavelengths that are separated in wavelength. For TOMS, we used wavelengths 331.2 and 360 nm. For SBUV/2, the photometer channel at 380 nm is used with the monochromator 331-nm channel. For OMPS, the 331 nm and 360 nm channels are available for both total and profile ozone products.

When one uses the R derived from 331 nm to calculate a radiance at 380 nm, the R- λ dependence produces a residue at 380 nm. This residue is positive when absorbing aerosols are present. By Mie scattering calculation, using various types of absorbing and non-absorbing aerosols, *Torres & Bhartia [1999]* showed that for the TOMS V7 algorithm a simple linear relationship between the residues and the O₃ error exists. Similar calculations using the TOMS V8TOZ algorithm indicate that O₃ is overestimated by $\sim 2.5 \pm 0.5$ DU when the 360-nm residue is 1%. The uncertainty represents variations in the estimated corrections due to aerosol type, their vertical distribution, and observational geometry. This means that in extreme cases, when the 360-nm residue reaches 10%, the maximum corrections are 25 ± 5 DU. We estimate that the error in this aerosol correction is 1.5%.

Mie scattering calculations show that the non-absorbing aerosols can also produce residues, but for reasons that are more conventional. It is well known that the optical depth of aerosols consisting of small particles varies as λ^{-A} , where A is called the Ångstrom coefficient and is typically close to 1. This produces a greater increase in UV radiances (above the Rayleigh background) at shorter wavelengths than at longer wavelengths, thus producing O₃ underestimation and a negative residue at 380 nm. However, compared to absorbing aerosols these effects are small. TOMS data indicate that 360-nm residues are rarely less than -2%. From Mie scattering calculation, the coefficient of correction comes out to be the same as for absorbing aerosols, *i.e.*, -2.5 DU for -1% residue at 360 nm.

Since relatively large residues, not related to aerosols, are seen at large solar zenith angles in the TOMS data, the aerosol correction is applied only when the solar zenith angle is less than 60°. TOMS data indicate that aerosol amounts are large enough to produce a 1% residue at 360

nm roughly 30% of the time, and most of these corrections are less than 5 DU. The larger OMPS NP FOV increases the portion of data with aerosols present.

Sun-Glint

The apparent reflectivity of the ocean in the BUUV in the glint direction (roughly a cone of $\pm 15^\circ$ from the nadir for the OMPS) varies with wavelength due to variations in the direct to diffuse ratio of the radiation falling on the surface. The magnitude of the sea-glint, and hence the $R-\lambda$ dependence it produces, decreases with increase in surface winds and by the presence of aerosols and clouds which also decrease the direct to diffuse ratio. Radiative transfer calculations [Ahmad & Fraser, private communication] show that, though the cause of the $R-\lambda$ dependence produced by sea-glint is quite different, its effect on O_3 and residuals is similar to that for absorbing aerosols, and the same correction procedure also applies. As mentioned in section 1.2.6, the nadir-viewing geometry of the OMPS and spacecraft orbits with equator crossing times more than an hour (15°) from solar noon limit the occurrence of sea glint geometries.

However, there is one aspect of sea-glint that is different from absorbing aerosols- the fact that they can significantly increase the apparent brightness of the surface and are easily confused with clouds. Since sea-glint increases the absorption of radiation by O_3 near the surface while clouds reduce the absorption, it is important to separate the two. The V8TOZ distinguishes clouds from sea-glint using the fact that clouds do not produce residues. So, in situations where geometry indicates the potential for sea-glint, retrievals with 360 nm residue greater than 3.5% are flagged as effected by sea-glint in the OMPS V8TOZ.

O_3 Profile

Strictly speaking, the BUUV radiances at all wavelengths have some sensitivity to the vertical distribution of O_3 . Though the wavelengths used in the V8TOZ algorithm to derive total O_3 have been selected to minimize this effect, and the step 2 correction procedure described in section 2.3.2 has been designed to correct any residual systematic errors, there are situations when the profile errors become too large to be acceptable. These situations begin to occur when the O_3 slant column density (SCD), $\Omega \times (\sec\theta + \sec\theta_0)$, exceeds 1500 DU. Studies of O_3 in the polar regions require that the algorithm be able to derive reasonable total O_3 values as close to the solar terminator as possible. At 80° solar zenith angle, the SCD can vary from less than 1000 DU to more than 4000 DU due to O_3 variability, and simply discarding data with very large SCD would seriously bias the zonal means. Therefore, it is important to design the algorithm such that reasonable (5%, 1σ) total O_3 values can be obtained for SCD of 5000 DU. From the error analysis of the TOMS algorithm [Wellemeyer et al., 1997], we have determined that errors at $SCD > 1500$ DU typically occur when the assumed O_3 profile near 10 hPa is significantly different from that assumed in step 2 (X_2). The error occurs because the algorithm has been explicitly designed (by using the standard profiles shown in Fig. 2-1) to minimize errors near 100 hPa where most of the O_3 variability takes place. This makes the algorithm sensitive to O_3 profile variations away from the 100 hPa region. Fig. 2-4 shows how a 10% error in the assumed profile between 4 hPa and 32 hPa (representing roughly 1σ variation of O_3 profile) affects the Step 2-derived total O_3 as a function of SCD.

Fortunately, profile errors near 10 hPa can be detected by examining the residue at shorter BUUV wavelengths which are more sensitive to O_3 profile than the wavelengths used for deriving total O_3 . Fig. 2-5 shows how the 312.5 nm residue responds to the profile error assumed for Fig. 2-4. More detailed analysis of this error using a set of O_3 profiles derived from high latitude

ozonesondes indicates that a simple correction factor of 3.5 DU for 1% residue at 312.5 nm provides adequate correction to obtain reliable total O₃ values (2%, 1σ) at SCDs of up to 3000 DU. However, the correction procedure becomes increasingly unreliable as the SCD exceeds 3000 DU.

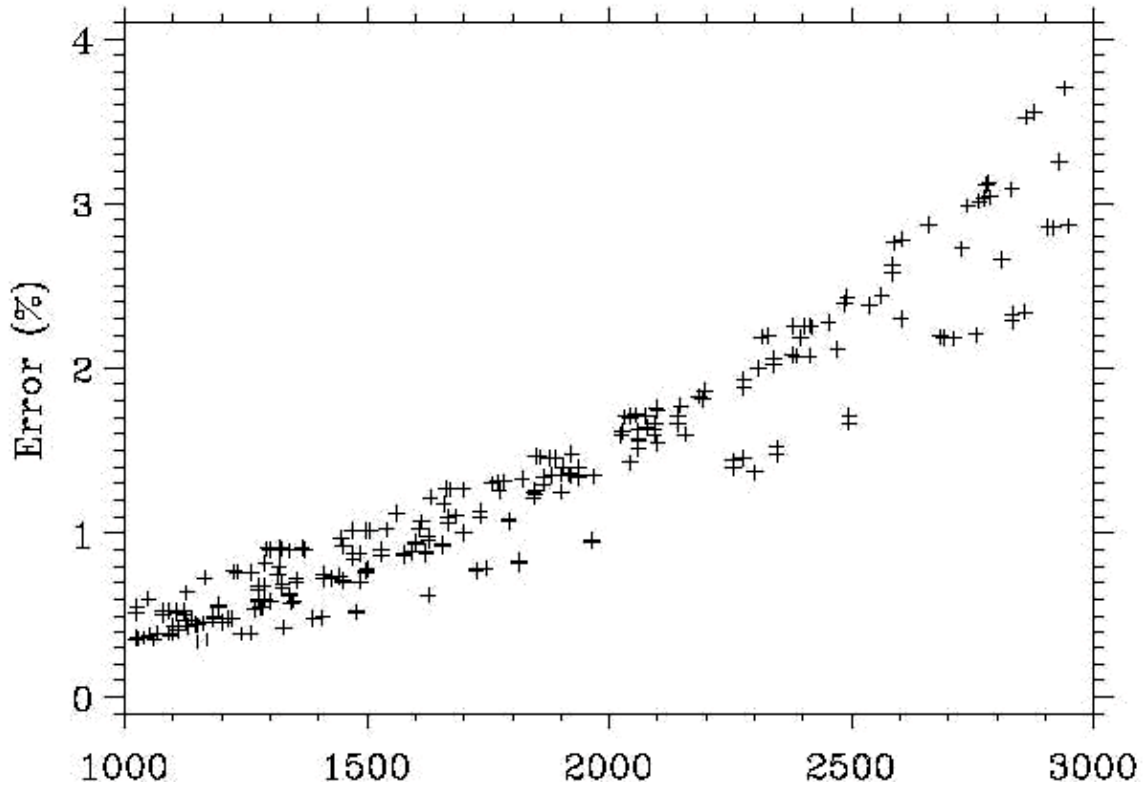


Figure 2-4: Error in retrieved total O₃ due to 10% more ozone in the 4 hPa to 32 hPa layer than assumed. The data shown are for the full range of solar

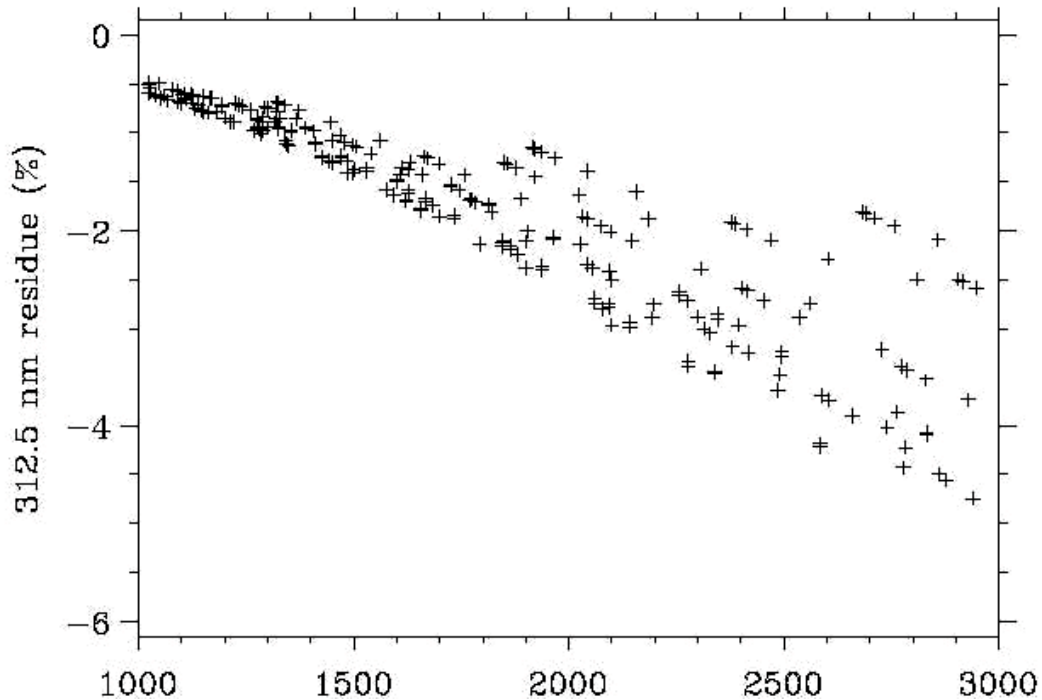


Figure 2-5: 312.5-nm residue for same profile errors as shown in Fig

For $SCD > 3000$ DU, OMPS uses the 360-nm channel to derive surface reflectivity, so that the 331-nm residue, which is fairly sensitive to total O_3 at these very high path lengths but insensitive to profile shape effects, can be used to identify error in the total O_3 derived using 317.5 nm. The residue based correction to the derived O_3 then is the product of the 331-nm residue and the total O_3 sensitivity at 331 nm, $\partial \ln I / \partial \Omega$.

Sulfur dioxide (SO_2)

As noted in section 1.2.3, SO_2 has strong absorption in the wavelengths used for the estimation of total O_3 . However, only volcanic SO_2 produces significant error in deriving total O_3 . Figure 2-6 shows the residues produced by a layer of SO_2 at 7.4 km (solid line) and 2.5 km (dotted line) containing 2.65×10^{16} molecules/cm² (1 DU), which will produce respectively 2.5 DU and 1.3 DU errors in deriving total O_3 using the V8TOZ algorithm. An SO_2 Index (SOI) is computed using a linear combination of the residues and absorption coefficients at four wavelengths 313, 318, 331, and 360 nm for Nimbus 7 and Meteor 3; and 318, 322, 331, and 360 nm for Earth Probe and ADEOS. The TOMS wavelengths were not chosen to optimize SO_2 retrieval, so the SOI is not a very precise parameter. If it exceeds a 5σ threshold, the associated O_3 retrieval is flagged as bad for SO_2 contamination. It should be noted that significant errors in total O_3 can occur for unflagged retrievals due to this lack of sensitivity. This is likely to occur in the vicinity of flagged retrievals caused by SO_2 emissions from volcanic eruptions. The OMPS NP version of the algorithm does not compute an SO_2 Index from the total O_3 wavelengths.

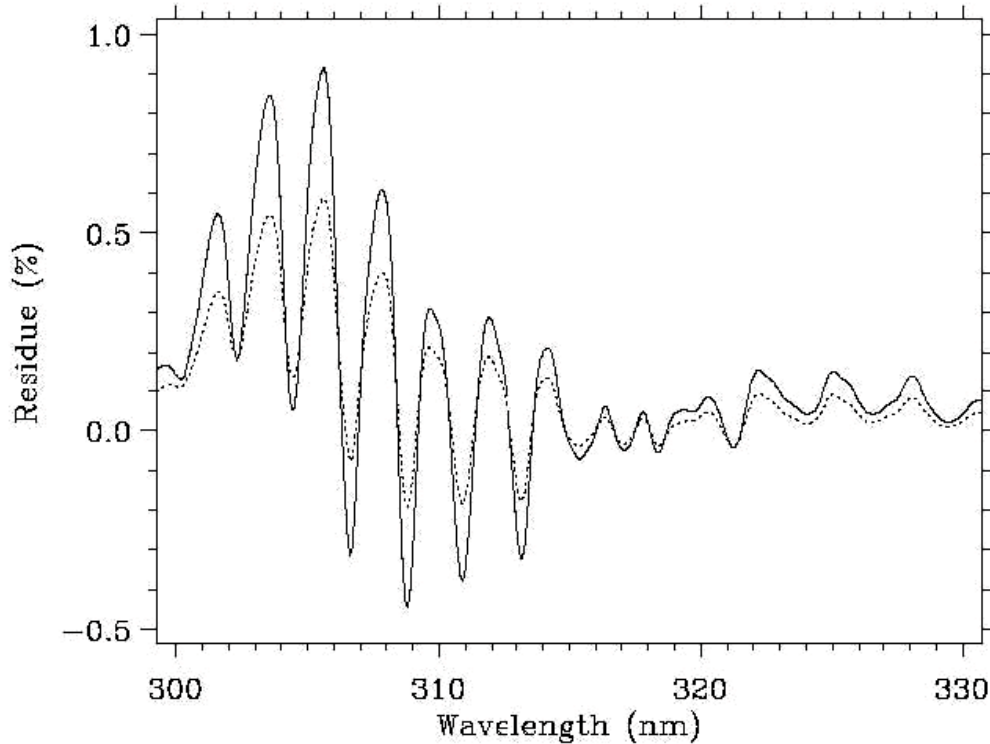


Figure 2-6: Residue caused by 1 DU of SO₂ column at 45° solar zenith angle,

2.4 Error Analysis

Like any remote sensing technique, the V8TOZ total O₃ algorithm is susceptible to three distinctly different types of error sources: 1) forward model errors, 2) inverse model errors, and 3) instrumental errors. In section 2.3.2 we discussed how we have designed the algorithm to minimize the impact of the first two of these errors by carefully constructing the O₃ and temperature profiles to remove any latitude and seasonally dependent biases from the data, and in section 2.3.3 we discussed how we use the residues to detect and correct errors that are localized in space and time. However, there are some errors that cannot be corrected by either of these methods. In this section we highlight these remaining errors. In addition, we discuss the sensitivity of the algorithm to instrumental errors.

2.4.1 Forward Model Errors

The forward model errors include errors that occur in the computation of radiances. Since even the best radiative transfer models can only approximate the complex scattering and absorption processes of the real atmosphere, one inevitably has errors. Since the retrieval algorithm essentially uses the difference between the measured and calculated radiances to derive O₃, errors in forward model calculations are just as important, if not more important (given that they are systematic), as errors in measured radiance. However, it is important to note that the algorithm uses a pair of wavelengths to derive O₃. Since these wavelengths are only 13 nm apart, relatively large errors in computing absolute radiances may not have much impact, while even small errors in computing the ratio of radiances become quite important. Following is a brief summary of key forward model errors.

Radiative Transfer Code

The TOMRAD radiative transfer code, the work-horse of the V8TOZ algorithm, assumes that the atmosphere contains only molecular scatterers and absorbers bounded by opaque Lambertian surfaces. Radiation amounts from these surfaces are linearly mixed to simulate the effect of clouds. Clearly, this scheme is an overly simplified treatment of many complex processes that occur in a real atmosphere, including Mie scattering by clouds and aerosols, scattering by non-spherical dust particles, and reflection by non-Lambertian surfaces. However, as discussed in the previous section, the ability of this code to simulate the ratio of radiances at weakly-absorbing wavelengths can be tested using TOMS data. These tests show that the prediction of forward model works quite well over a very large range of conditions, with three key exceptions, two of which we have already noted: sea-glint and UV-absorbing aerosols. The third case usually occurs at large solar zenith angles in the presence of snow/ice, where the forward model underestimates the ratio of 340-nm/380-nm radiances by several percent. If this anomaly is caused by the presence of clouds over bright surfaces, as is strongly suspected, its impact on derived O₃ would be small, since multiple scattering between the surface and clouds reduces the shielding effect of clouds.

Analysis of the ratio of 340-nm and 380-nm radiances, however, leaves out the possible effect of clouds, aerosols and surfaces in changing the absorption of radiation by O₃. To understand these effects, we use a more realistic radiative transfer model in which we assume that clouds are homogeneous and plane-parallel layer of Mie scatterers. We calculate the effect of clouds on the BUV radiances using the Gauss-Seidel vector code [*Herman & Browning, 1965*] using Deirmendjian's [*Deirmendjian, 1969*] C1 cloud model. By varying the cloud optical depth in this model one can produce a curve similar to that shown in Fig. 2-2. Comparison with TOMS data shows similar good agreement, which leads us to believe that this model is a reasonable way to model cloud effects in UV, with the advantage that one can account for surface-cloud interactions that the operational model ignores. However, detailed comparison of the results from the two models indicates that despite their drastically different characterization of clouds, the total O₃ derived from these models are essentially the same (within $\pm 1\%$), provided one uses the correct effective pressure of the clouds. (The effective pressure of the cloud is usually greater, *i.e.*, the clouds scattering emanates from lower altitude, than the cloud top pressure, depending upon the optical and physical thickness of the clouds, surface albedo and observation geometry. It is expected that UV or visible cloud algorithms would provide a more accurate value of this pressure than infrared algorithms, which sense the black-body temperature of cloud-tops, for all but very thin clouds, such as cirrus.)

This error analysis does not apply to clouds and aerosols in the stratosphere, which can significantly alter the absorption of the BUV radiation by stratospheric O₃, producing relatively large errors. It has been shown [*Torres et al., 1992; Bhartia et al., 1993*] that at high solar zenith angles ($\theta_0 > 80^\circ$) stratospheric clouds (*e.g.*, PSCs) and aerosols may cause the total O₃ to be significantly underestimated, provided they are sufficiently optically thick ($\tau > 0.1$) and are close to the O₃ density peak. This is because the photons scattered in the stratosphere do not sense the entire O₃ column. However, at lower solar zenith angles, the error can be either positive or negative and may vary in a complicated way with observation geometry. Though it is known that optically thick Type III PSCs containing water ice do form due to adiabatic ascent of air as it passes over orographic features (lee waves), sometimes creating localized O₃ depletion called a "mini-hole", it is not known if the optical depth of these clouds is large enough, or if they are high enough, to produce the errors postulated by *Torres et al. [1998]*. However, the effects of

high altitude stratospheric aerosols that form after volcanic eruptions are well understood [Torres et al., 1995]. Bhartia et al. [1993] estimate that the stratospheric aerosols created few months after the 1991 eruption of Mt. Pinatubo volcano in the Philippines introduced errors in the BUV total O₃ retrieval of +6 to -10%, depending on solar zenith angle, though these errors subsided quickly after 6 months as the altitude of the aerosols dropped.

To summarize, under normal circumstances for OMPS, the radiative transfer modeling errors would contribute approximately 1.5% (1 σ) error in the computation of O₃. However, in the presence of Type III PSCs, and for several months after high altitude volcanic eruptions, the errors may be an order of magnitude larger.

Spectroscopic Constants

Several groups have made measurements of O₃ absorption cross-sections recently. Based on evaluation of Bass & Paur [1984] measurements by Chance [private communication], it is estimated that at the wavelengths used to derive total O₃ (317.5 nm) Bass and Paur measurements are probably accurate to better than 2%. We have used the Bass and Paur measurements shortward of 340 nm, and FTS Measurements from University of Bremen [S. Voight, private communication, 2001]. Uncertainty in molecular scattering cross-sections are generally considered small (<1%), and in any case the errors are not likely to vary significantly with wavelength to affect derived total O₃. Some non-physical values for the temperature dependence of the O₃ cross-sections have been found in the Bass and Paur data sets and alternative sources are under evaluation.

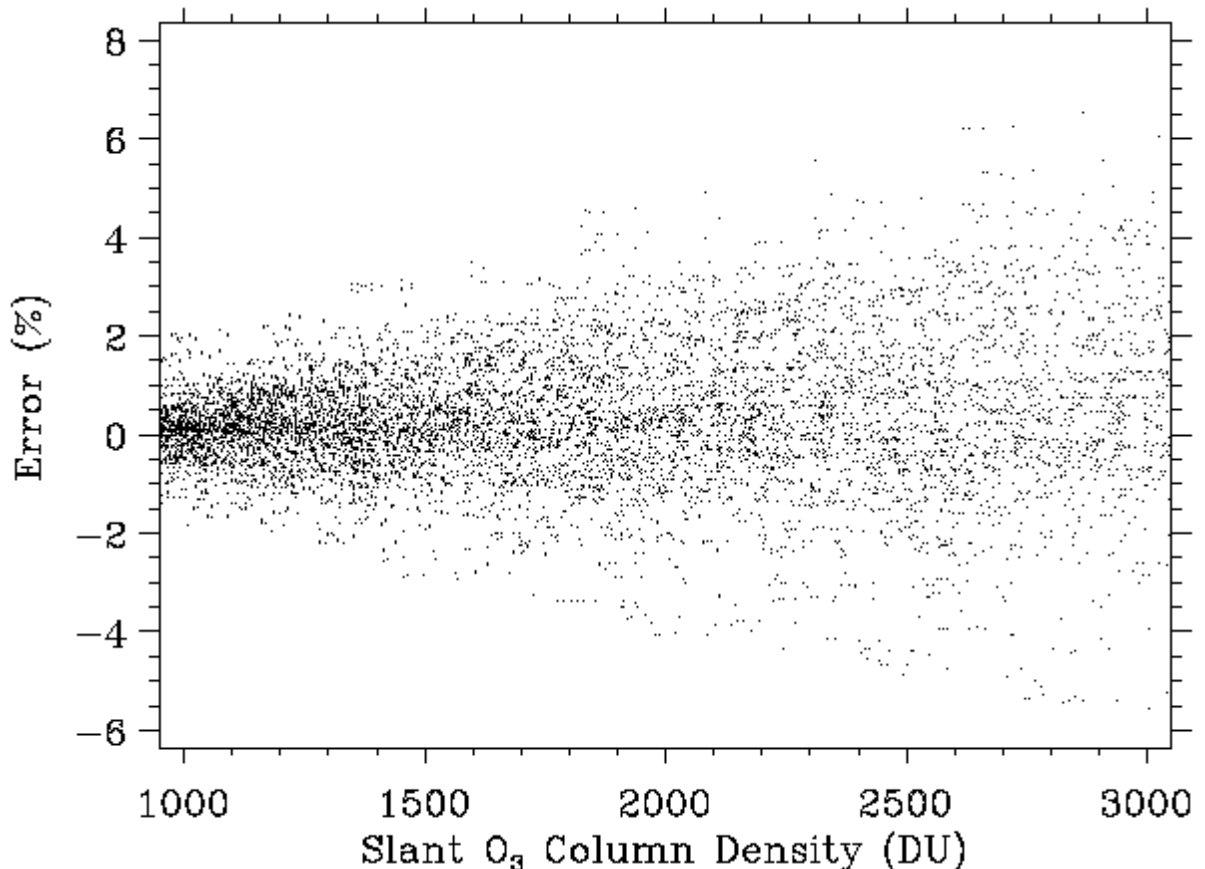
2.4.2 Inverse Model Errors

In remote sensing problems, the inverse model errors are caused by the fact that the inversions of radiances into geophysical parameters require *a priori* information. This is true of even the simplest type of remote sensing, *e.g.*, measurement of total O₃ using direct solar radiation, as employed by ground-based Dobson and Brewer instruments. The inversion algorithms for these instruments require some knowledge of how the O₃ is distributed vertically in the atmosphere in order to correct for the effects of atmospheric temperature on O₃ absorption cross-section, and for the effect of Earth's sphericity on the airmass factor. Errors in *a priori*, therefore, inevitably introduce retrieval errors; though for Dobson and Brewer algorithms they are usually quite small (<1%). The following is a summary of these errors for the V8TOZ algorithm.

O₃ Profile

As discussed in section 2.3, the V8TOZ algorithm uses an elaborate scheme to minimize errors due to the O₃ profile shape. To understand the residual errors, it is convenient to divide the atmosphere into 3 regions: lower troposphere (LT, surface-5 km), upper troposphere and lower stratosphere (UTLS, 5-25 km), and middle stratosphere (MS, 25-40 km). (O₃ amounts above 40 km are too small to be a significant error source.) Detailed analysis of errors from these three regions indicates that at SCD<1500, the LT region is by far the most important error source. This occurs because the BUV radiation loses sensitivity to the LT region due to strong molecular scattering, which can be reduced further by mid/high level clouds. On the average, at solar zenith angles less than 70°, the sensitivity to O₃ changes in this region is roughly half compared to the regions above. This is one of the primary reasons for the step 2 correction described in section 2.3.2, which is designed to reduce any seasonal and latitudinal bias resulting from this error. However, since the O₃ in the LT region has short-term variability of about 5 DU (1 σ), one expects 2.5 DU (1 σ) error in derived total O₃ from this source alone.

Surprisingly, given the large variability of the O₃ profile in this region, additional error caused by the UTLS region remains quite small even up to very large solar zenith angles. Fig. 2-7 shows the combined errors from the variability of O₃ profiles below 22 km estimated using data from the Sodankylä ozonesonde station (67.4°N, 26.6°E). As a function of solar zenith angle, the standard deviation of error remains less than 2% up to 81°, increasing to only 3.1% at 86°. Such small errors are a direct result of the method we have used to construct the profiles for retrieval, as described in section 2.3.2. It is easy to show that less careful methods of constructing the profiles, employed by many DOAS algorithms, would cause the errors from the UTLS region to increase rapidly at large solar zenith angles.



At SCD > 1500 DU, the profile effect of the MS region starts to become important. However, error analysis using high latitude O₃ profiles obtained from satellites indicate that the step 3 profile correction (described in section 2.3.3) works quite well. The residual errors are estimated to be ~1.5% (1 σ), increasing to 5% at SCD of 5000 DU. If the maximum-likelihood-estimation procedure is employed, then these errors can be reduced further. Total RMS errors due to variations in the O₃ profile are: ~1.5% up to 70° solar zenith, ~3% at 82° and ~5% at 85°.

Temperature Profile

Step 2 of the algorithm corrects for seasonal and latitudinal variation of the atmospheric temperature. Residual errors are less than 0.5% (1 σ). Though the errors can become larger in the polar regions, the O₃ profile errors remain the dominant error source at all latitudes. Therefore, at present, we do not see any need to bring in daily temperature maps to improve our total O₃ estimates.

2.4.3 Instrumental Errors

Instrumental errors include systematic errors due to pre-launch errors in instrument calibration (spectral and radiometric), calibration drift after launch, and random noise. Since we do not yet know how large these errors are likely to be, we provide sensitivity to various errors in the following.

Spectral Calibration

The 317.5-nm wavelength channel is located on a plateau in the O₃ absorption cross-section; hence it is not particularly sensitive to wavelength errors: a 0.01-nm error in wavelength produces 0.1% error in O₃. This is roughly the uncertainty in the OMPS wavelength scale calibration.

Radiometric Calibration

Unlike DOAS algorithms, the V8TOZ algorithm is quite sensitive to radiometric calibration errors. A 1% calibration error, independent of wavelength between 317.5 nm and 331.2 nm, introduces a 0-2 DU O₃ error depending on brightness of the scene. (Larger errors occur for darker scenes.) A 1% relative calibration error between the two wavelengths introduces ~4-6 DU error depending on slant column O₃ amount. (The smallest errors occur at SCD of ~1000 DU.) Over the years, several strategies have been developed to detect the calibration errors by the analysis of residues. We estimate that the radiometric calibration of an individual OMPS total O₃ or reflectivity is accurate to 1%, and may contain drifts of 1%/decade or less after retrospective characterization. Operational variations for total O₃ channels may reach 2%.

Instrument Noise

A 1% instrument noise at each of the two wavelengths used for total O₃ retrieval would lead to 6 DU to 9 DU noise in total O₃. The noise of the OMPS instrument in total O₃ and reflectivity channels is ten times better than this, so its effect will be well below the systematic errors and therefore of little significance.

2.4.4 Error Summary

All the important error sources we have discussed above are systematic, *i.e.*, the errors are repeatable given the same geophysical conditions and viewing geometry. However, most errors vary in a pseudo-random manner with space and time, so they tend to average out when data are averaged or smoothed. The best way to characterize these errors is as follows: the errors at any given location would have a roughly Gaussian probability distribution with standard deviation of about 2% at solar zenith angles less than 70°, increasing to 5% at 85°, with a non-zero mean. The means themselves will have a roughly Gaussian distribution with standard deviation of about 1% with non-zero mean of ±2% (due to error in O₃ absorption cross-section). Conservatively, one should assume that the latter error distribution is not affected by the amount of smoothing, *i.e.*, it remains the same whether one looks at monthly mean at any given location, daily zonal mean, monthly zonal mean, or even yearly mean

2.4. Algorithm Output

Describe the output data products - not format - at a level of detail to determine if the product meets user requirements. (*Document Object 17*)

Writers: Algorithm Scientists.

Table 1-2 describes the external distributed NDEV8T file and Table 1-3 lists its content. Details of the derivation of all of the products are described in the NDE Version 8 Total Ozone Algorithm Theoretical Basis Document.

Table 1-3 describes the variables in file. The ozone total column is defined as the amount of Ozone in a vertical column of the atmosphere measured in Dobson Units (1 DU = 1 milli-atm-cm). The key EDR product is the ColumnAmountO3 estimate.

Table 2-1 NDE Total Column Ozone File

File	Description	Format	Size/file
V8TOZ-EDR_v1r0_npp_s201601120127494_e201601120128268_c201603221503000.nc	This is the granule output file containing all the derived variables of the NDEV8T product.	netCDF4	0.8 MB/granule file, ~1009 files/day

Table 2-2 Total Column Ozone Output Granule File Content

Name	Type	Description	Dimension	Units	Range
Latitude	32 bit Float	Latitude	15 x 105	Degrees	-90 ~ 90
Longitude	32 bit Float	Longitude	15 x 105	Degrees	-180 ~ 180
SolarZenithAngle	32 bit Float	Solar Zenith Angle	15 x 105	Degrees	0 ~ 180
SatelliteViewAngle	32 bit Float	Satellite View Angle	15 x 105	Degrees	-90~ 90
RelativeAzimuth	32 bit Float	Relative Azimuth	15 x 105	Degrees	-180~ 180
AerosolIndex	32 bit Float	Aerosol Index	15 x 105	Unitless	-100~ 100
AlgorithmFlag	32 bit	Algorithm Flag	15 x 105	Unitless	0 ~ 10

	Integer				
CloudFraction	32 bit Float	Cloud Fraction	15 x 105	Unitless	0~ 1
CloudTopPressure	32 bit Float	Pressure at top of cloud	15 x 105	hPa	10~ 2000
ColumnAmountO3	32 bit Float	V8TOZ Total Column of Ozone	15 x 105	Dobson Units	0~ 1000
EclipseFlag	32 bit Float	Eclipse Flag	15 x 105	Unitless	0~ 10
ErrorFlag	32 bit Integer	Error Flag	15 x 105	Unitless	0~ 10
O3BelowCloud	32 bit Float	Total Column of Ozone below Cloud	15 x 105	Dobson Units	0~ 1000
QualityFlag	32 bit Integer	Quality Flag	15 x 105	Unitless	0~ 10
Reflectivity331	32 bit Float	Average 331 nm Reflectivity from V8TOz retrieval	15 x 105	%	0~ 100
Reflectivity360	32 bit Float	Average 360 nm Reflectivity from V8TOz retrieval	15 x 105	%	0~ 100
So2Index	32 bit Float	So2 Index	15 x 105	Unitless	-100~ 100
Step1Ozone	32 bit Float	V8TOZ Step1 Ozone	15 x 105	Dobson Units	0~ 1000
Step2Ozone	32 bit Float	V8TOZ Step2 Ozone	15 x 105	Dobson Units	0~ 1000
SunGlintFlag	32 bit Float	Sun Glint Flag	15 x 105	Unitless	0~ 10
NvalueAdjustment	32 bit Float	N-Value adjustment for 12 V8TOZ wavelengths	105 x 12	N-Values	-20~ 20
NvalueMeasured	32 bit Float	V8TOZ Measured normalized radiances for 12 V8TOZ wavelengths	15 x 105 x 12	N-Values	0~ 100
Step1Residual	32 bit	V8TOZ Step 1	15 x 105 x 12	N-Values	-50~ 50

	Float	Residuals			
Step2Residual	32 bit Float	V8TOZ Step 2 Residuals	15 x 105 x 12	N-Values	-50~ 50
Step3Residual	32 bit Float	V8TOZ Step 3 Residuals	15 x 105 x 12	N-Values	-50~ 50
dNdOmega	32 bit Float	V8TOz ozone sensitivities	15 x 105 x 12	N- Value/Do bson unit	-20~ 50
dNdR	32 bit Float	V8TOz reflectivity sensitivities	15 x 105 x 12	N-Values	0~ 600
LayerEfficiency	32 bit Float	V8TOz Layer retrieval efficiencies	15 x 105 x 11	DU/DU	-1~ 10
TemperatureProfile	32 bit Float	Temperature Profile	15 x 105 x 11	Degrees Kelvin	100~ 400
Step2Profile	32 bit Float	Step2 Ozone Profile	15 x 105 x 11	Dobson Units	10~ 400
TerrPressure	32 bit Float	Terrain Pressure from LUT	15 x 105	hPa	100~ 1500
Wavelengths	32 bit Float	12 Wavelengths of Observation for V8TOz	12	nm	300~ 420
ScanTime	62 bit Float	Elapsed time in seconds since Jan 1, 1958 including leap seconds	15	Microsec onds	1.0~ 1.0E12
Ascending_Desce nding	32 bit Integer	1=Descending, 0=Ascending	15	Unitless	0~ 1
quality_informati on	8 bit Chara cter	Granule quality information	1	%	0.0~ 100.0
38 V8TOZ diagnostic variables	See netCD F4 metad ata	Variables to describe observing and environmen tal conditions, and results of algorithm tests	38	See netCDF4 metadata	See netCDF4 metadata

2.5. Performance Estimates

2.5.1. Test Data Description

The V8TOz algorithm has been used to process the five years (2012-2016) of S-NPP OMPS NM SDRs. Analysis of the results are provided at https://www.star.nesdis.noaa.gov/smcd/spb/OMPSDemo/proOMPSbeta.TOZ_V8.php and have been use to provide the performance estimates present in the readiness reviews and in this section. These results used the operational SDR products so the quality of the measurements have been improving as the SDR algorithms are updated. The V8TOz algorithm is already in use with the GOME-2 measurements to create operational total ozone products at OSDPD. It has also been used to process over ten years of NASA EOS AURA OMI measurements.

2.5.2. Sensor Effects

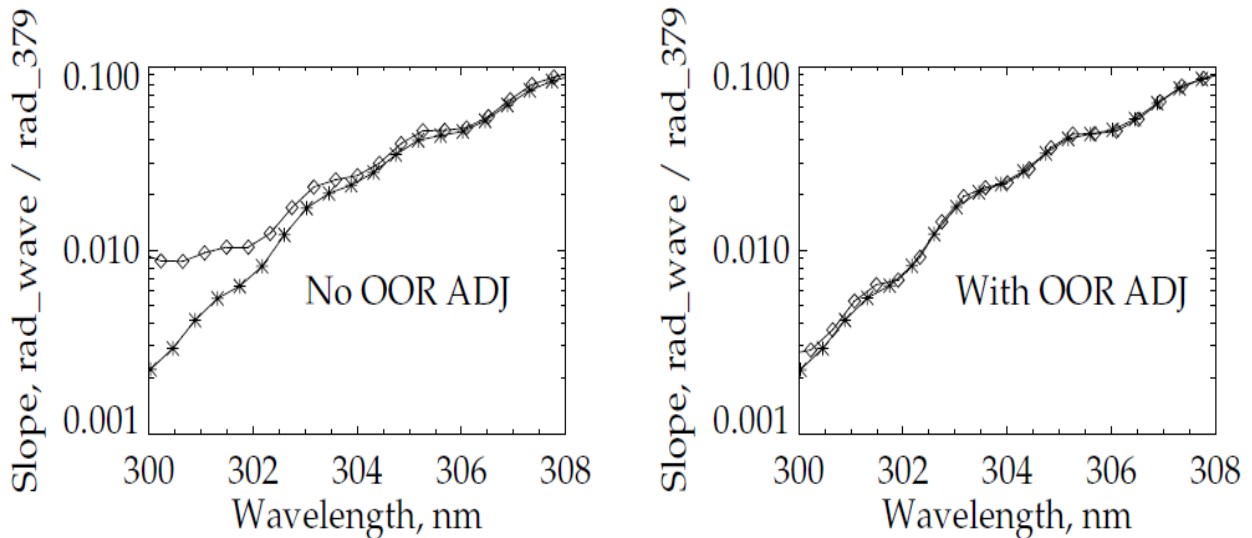
The OMPS NM SDR has very good corrections for stray light, dark current, non-linearity and intra-orbital wavelength scale drift.

Table 2.5 OMPS NADIR SDR Performance Requirements

Parameter	Requirement	Comments
A. Wavelength range (Profile) B. Wavelength range (Total)	250 to 340 nm 300 to 420 nm	A. Ozone profile, column and UV reflectivity. B. Total column ozone and path length range, UV reflectivity, aerosol index leverage, stray light monitoring, solar features for Ring effect.
Bandwidth (FWHM)	< 1.1 nm	Discrete channels, ozone absorption and solar line resolution.
Samples/FWHM	> 2.3	A. λ -shift, Mg II Index, additional channels will be used to reduce noise for smaller FOVs. B. λ -shift, Ring effect, Multiple pairs for O3, additional wavelengths for SO2, intervals for Cloud Optical Centroid.
Polarization sensitivity	< 5%	Accuracy
λ -registration	< 0.01 nm	O ₃ and SO ₂ Absorption gradients and solar registration and variability
A. Horizontal cell size (Profile) B. Horizontal cell size (Total)	< 50 km @ nadir < 17 km @ nadir	Product FOV sizes and oversampling.
A. Horizontal coverage (Profile) B. Horizontal coverage (Total)	> 250 km > 2800 km	A. Weekly Revisit. B. Daily global coverage

A. Pixel to pixel calibration (Profile) B. Pixel to pixel calibration (Total)	< 1% < 0.5%	Accuracy (includes non-linearity)
Albedo calibration	< 2%	Accuracy and stability
A. Albedo deviation error (Profile) B. Albedo deviation error (Total)	< 2% < 1%	Accuracy and stability
A. Signal-to-Noise Ratio (Profile) B. Signal-to-Noise Ratio (Total)	See Table 4.4.2.2 > 300 for SZA < 80°	A. Precision for 250 km FOV and 38 Second integration at minimum radiances. B. Precision for pixel bin factor of four and 1 Second integration, for 305 – 380 nm at min. radiance.
Stray light (out-of-band)	< 1%	A. For critical channels in Table 4.4.2.2, after applying correction. B. For 305 to 380 nm. <2% for other channels, after applying correction.
		v2.10, 1/24/14

The stray light was well characterized prelaunch and the measurements were used to develop a scene-based source to target correction. Correlation analysis confirms the removal of most stray light errors. The figures below show the without and with Out-Of-Range corrections results for the OMPS Nadir Mapper compared to the OMPS Nadir Profiler correlations. The OMPS Nadir Profiler measurements are taken after passing through a dichroic filter so they have very low stray light contamination.



The dark current errors are reduced to low levels by making weekly updates to the dark lookup table. The non-linearity correction has been kept at pre-launch values, as the bi-weekly monitoring has not shown any significant changes. Similarly, the instrument

throughput has been very stable as monitored by the bi-annual reference solar measurements.

A wavelength scale variation correlated the orbital variation in temperature gradients has been identified. Measurement-based estimates of the wavelength shifts are made for every granule for every cross track position and the results are provided in the SDR. The uncertainty of these estimates is smaller than 0.005 nm.

2.5.3. Retrieval Errors

EDR Attribute	Threshold
Ozone TC Applicable Conditions:	
1. Threshold requirements only apply under daytime conditions with Solar Zenith Angles (SZA) up to 80 degrees.	
2. The EDR shall be delivered for all SZA.	
a. Horizontal Cell Size	50 x 50 km ² @ nadir
b. Vertical Cell Size	0 - 60 km
c. Mapping Uncertainty, 1 Sigma	5 km at Nadir
d. Measurement Range	50 - 650 milli-atm-cm
e. Measurement Precision	
1. X < 0.25 atm-cm	6.0 milli-atm-cm
2. 0.25 < X < 0.45 atm-cm	7.7 milli-atm-cm
3. X > 0.45 atm-cm	2.8 milli-atm-cm + 1.1%
f. Measurement Accuracy	
1. X < 0.25 atm-cm	9.5 milli-atm-cm
2. 0.25 < X < 0.45 atm-cm	13.0 milli-atm-cm
3. X > 0.45 atm-cm	16.0 milli-atm-cm
g. Refresh	At least 90% coverage of the globe every 24 hours (monthly average)

Verification of Performance:

- (a) 20-Pixel Aggregation and 7-S along track integration.
- (b) 318 nm channel BUUV comes from surface to top of atmosphere.
- (c) Confirmed by coastlines and comparison to 750 m VIIRS.
- (d) Confirmed by standard profiles and four years of processing.

(e) Precision estimates from Nearest Neighbor analysis.

(f) Accuracy is adjusted by soft calibration,

(g) 105° cross-track swath provides full daily coverage.

Figures are provide in the V8TOZ Algorithm Readiness Review.

2.5.3.1. Practical Considerations

The main sources of errors are from the forward model, noted in Section 2.3, due to uncertainties in determining the cloud and aerosol properties and differences between the real and standard profiles. The measurement calibration bias effects are taken out by using soft-calibration adjustments.

2.5.4. Numerical Computation Considerations

The use of table interpolation to obtain forward model estimates of albedos and their sensitivities to parameters allow for very efficient retrievals. Double precision calculations maintain keep computational errors well below other sources of uncertainty.

2.5.5. Programming and Procedural Considerations

The algorithm is straightforward in its progression through the three ozone steps and the logical test and computational mathematics are basic algebra and trigonometry.

2.5.6. Quality Assessment and Diagnostics

The product quality is monitored at

https://www.star.nesdis.noaa.gov/smcd/spb/OMPSDemo/proOMPSbeta.TOZ_V8.php

for the EDR products and at

https://www.star.nesdis.noaa.gov/icvs/status_NPP_OMPS_NM.php

for the SDR products. The products progress through the standard validation from beta, to provisional, to validated stages 1, 2 and 3.

2.5.7. Exception Handling

The algorithm checks for non-physical values for radiances and returns a set of fill values for any retrieval encountering difficulties. The V8TOz algorithm has known deficiencies for high levels of atmospheric SO₂ or aerosols. Both conditions are identified and flagged by checking the values of measurement based residuals.

2.6. Validation

The V8TOZ algorithm has been used as a component of the V8Pro operational algorithm for the NOAA POES SBUV/2 instruments since 2000. It has also been used since 2008 as the operational algorithm for the NOAA processing of the EUMETSAT GOME-2 instrument measurements.

3. ASSUMPTIONS AND LIMITATIONS

3.1. Performance Assumptions

The algorithm meets product performance requirements for products up to 80° solar zenith angles. It continues to generate products but with increased uncertainty out to 88°. The algorithm also flags eclipse conditions, which lead to poor performance as the solar signal reduction is complex.

3.2. Potential Improvements

The V8TOz suffers from significant errors when there are elevated levels of atmospheric SO₂. An algorithm, called the Linear Fit SO₂ algorithm uses the V8TOz residuals and the sensitivity of the measurements to SO₂ absorption, to make estimates of the atmospheric SO₂ and then generates adjustments to the total column ozone estimates. We are implementing this algorithm as a follow-on process for the V8TOz.

The algorithm can make use of more channels than the current 12 used directly. The main benefit of the additional channels is a reduction in the effects of measurement noise. This can be accomplished by using information concentration methods such as principal component analysis or simple polynomial regression over wavelength intervals about given channels.

4. REFERENCES

List all references to external documents.

2.5 References

- Ahmad, Z. & P.K. Bhartia, "Effect of Molecular Anisotropy on the Backscattered UV Radiance," *Appl. Opt.*, **34**, 8309-8314, 1995.
- Bass, A.M. & R.J. Paur, "The ultraviolet cross-section of ozone: I The measurements," in *Atmospheric Ozone*, edited by C.S. Zerefos and A. Ghazi, 606-610, D. Reidel, Norwood, Mass., 1984.
- Bates, D. R., "Rayleigh scattering by air," *Planet. Space Sci.*, **32**, 785-790, 1984.
- Bhartia, P.K., *et al.*, "Effect of Mount Pinatubo Aerosols on Total Ozone Measurements From Backscatter Ultraviolet (BUV) Experiments," *J. Geophys. Res.*, **98**, 18547-18554, 1993.
- Bhartia, P.K., *et al.*, "Algorithm for the Estimation of Vertical Ozone Profile from the Backscattered Ultraviolet (BUV) Technique," *J. Geophys. Res.*, **101**, 18793-18806, 1996.
- Bhartia, P. K., McPeters, R. D., Flynn, L. E., Taylor, S., Kramarova, N. A., Frith, S., Fisher, B., and DeLand, M.: Solar Backscatter UV (SBUV) total ozone and profile algorithm, *Atmos. Meas. Tech.*, **6**, 2533-2548, doi:10.5194/amt-6-2533-2013, 2013.
- Brion, J., *et al.*, "High-resolution laboratory absorption cross section of O₃. Temperature effect," *Chem. Phys. Lett.*, **213** (5-6), 610-512, 1993.
- Caudill, T.R., *et al.*, "Evaluation of the pseudo-spherical approximation for backscattered ultraviolet radiances and ozone retrieval," *J. Geophys. Res.*, **102**, 3881-3890, 1997.
- Chance, K., & R.J.D. "Spurr, Ring Effect Studies: Rayleigh Scattering, Including Molecular Parameters for Rotational Raman Scattering, and the Fraunhofer Spectrum," *Applied Optics* **36**, 5224-5230, 1997.
- Deirmendjian, D., *Electromagnetic scattering on spherical polydispersions*, Elsevier, 290, 1969.
- Dave, J. V., "Meaning of successive iteration of the auxiliary equation of radiative transfer," *Astrophys. J.*, **140**, 1292-1303, 1964.
- Dave, J.V. & C.L. Mateer, "A preliminary study on the possibility of estimating total atmospheric ozone from satellite measurements," *J. Atmos. Sci.*, **24**, 414-427, 1967.
- Dave, J.V., "Effect of Aerosols on the estimation of total ozone in an atmospheric column from the measurements of its ultraviolet radiance," *J. Atmos. Sci.*, **35**, 899-911, 1978.
- Eck, T.F., *et al.*, "Reflectivity of the Earth's Surface and Clouds in Ultraviolet from Satellite Observations," *J. Geophys. Res.*, **92**, 4287, 1987.
- Fishman, J., *et al.*, "Use of satellite data to study tropospheric ozone in the tropics," *J. Geophys. Res.*, **91**, 14,451-14,465, 1986.
- Greenblatt, G.D., *et al.*, "Absorption Measurements of Oxygen Between 330 and 1140 nm," *J. Geophys. Res.*, **95**, 18,577-18,582, 1990.

-
- Grainger, J.F. & J. Ring, "Anomalous Fraunhofer line profiles", *Nature*, **193**, 762, 1962.
- Herman, B.M., & S.R. Browning, "A numerical solution to the equation of radiative transfer," *J. Atmos. Sci.*, **22**, 559-566, 1965.
- Herman, J.R., & E.A. Celarier, "Earth surface reflectivity climatology at 340-380 nm from TOMS data," *J. Geophys. Res.*, **102**, 28003-28011, 1997.
- Joiner, J., *et al.*, "Rotational-Raman Scattering (Ring Effect) in Satellite Backscatter Ultraviolet Measurements," *Appl. Opt.*, **34**, 4513-4525, 1995.
- Joiner, J. & P.K. Bhartia, "The Determination of Cloud Pressures from Rotational-Raman Scattering in Satellite Backscatter Ultraviolet Measurements," *J. Geophys. Res.*, **100**, 23019-23026, 1995.
- Joiner, J. & P.K. Bhartia, "Accurate determination of total ozone using SBUV continuous spectral scan measurements," *J. Geophys. Res.*, **102**, 12,957-12,970, 1997.
- Joiner, J., *et al.*, "Rotational-Raman Scattering (Ring Effect) in Satellite Backscatter Ultraviolet Measurements," *Appl. Opt.*, **34**, 4513-4525, 1995.
- Kattawar, G.W., A.T. Young, & T.J. Humphreys, "Inelastic scattering in planetary atmospheres. I. The Ring Effect, without aerosols," *Astrophys. J.*, **243**, 1049-1057, 1981.
- Klenk, K.F., *et al.*, "Total ozone determination from the Backscattered Ultraviolet (BUV) experiment," *J. Appl. Meteorol.*, **21**, 1672-1684, 1982.
- Koelemeijer, R.B.A., & P. Stammes, "Effects of clouds on ozone column retrieval from GOME UV measurements," *J. Geophys. Res.*, **104**, 8,281-8,294, 1999.
- Krueger, A.J., "Sighting of El Chichon Sulfur Dioxide with the Nimbus-7 Total Ozone Mapping Spectrometer," *Science*, **220**, 1377-1378, 1983.
- Mateer, C.L., D.F. Heath, & A.J. Krueger, "Estimation of total ozone from satellite measurements of backscattered ultraviolet Earth radiance," *J. Atmos. Sci.*, **28**, 1307--1311, 1971.
- McPeters, R.D., D.F. Heath, & B.M. Schlesinger, "Satellite observation of SO₂ from El Chichon: Identification and Measurement," *Geophys Res. Lett.*, **11**, 1203-1206, 1984.
- McPeters, R.D., "Climatology of Nitric Oxide in the upper stratosphere, mesosphere, and thermosphere: 1979 through 1986," *J. Geophys. Res.*, **94**, 3461-3472, 1989.
- McPeters, R.D. *et al.*, Nimbus-7 Total Ozone Mapping Spectrometer (TOMS) Data Products User's Guide, NASA Reference Publication 1384, 1996.
- McPeters, R.D., J.A. Logan, & G.J. Labow, "Ozone Climatological Profiles for Version 8 TOMS and SBUV Retrievals." A21D-0998, AGU Fall 2003.
- Seftor, C. J., G. Jaross, M. Kowitt, M. Haken, J. Li, and L. E. Flynn (2014), Postlaunch performance of the Suomi National Polar-orbiting Partnership Ozone Mapping and Profiler Suite (OMPS) nadir sensors, *J. Geophys. Res. Atmos.*, **119**, 4413–4428, doi:[10.1002/2013JD020472](https://doi.org/10.1002/2013JD020472).
- Thomas, G.E., "Solar Mesosphere Explorer measurements of polar mesospheric clouds (noctilucent clouds)," *J. Atmos. Terr. Phys.*, **46**, 819-824, 1984.
- Thomas, G.E., "Climatology of polar mesospheric clouds: Interannual variability and implications for long-term trends," *Geophysical Monograph* **87**, AGU, 1995.

-
- Torres, O. & P.K. Bhartia, "Effect of Stratospheric Aerosols on Ozone Profile from BUUV Measurements," *Geophys. Res. Lett.*, **22**, 235-238, 1995.
- Torres, O., Z. Ahmad & J.R. Herman, "Optical effects of polar stratospheric clouds on the retrieval of TOMS total ozone," *J. Geophys. Res.*, **97**, 13015-13024, 1992.
- Torres, O., *et al.*, "Properties of Mt. Pinatubo Aerosols as Derived from Nimbus-7 TOMS Measurements," *J. Geophys. Res.*, **100**, pp. 14,043-14,056, 1995.
- Torres, O., *et al.*, "Derivation of aerosol properties from satellite measurements of backscattered ultraviolet radiation: Theoretical basis," *J. Geophys. Res.*, **103**, 17,099-17,110, 1998.
- Torres, O. & P.K. Bhartia, "Impact of tropospheric aerosol absorption on ozone retrieval from backscattered ultraviolet measurements," *J. Geophys. Res.*, **104**, 21569-21,577, 1999.
- Voigt, S., *et al.*, "The temperature dependence (203293 K) of the absorption cross sections of O₃ in the 230-850 nm region measured by Fourier-Transform spectroscopy," *J. Photochem. Photobiol. A*, **143**, 1-9, 2001.
- Vountas, M., V.V. Rozanov & J.P. Burrows, "Ring Effect: Impact of rotational Raman scattering on radiative transfer in Earth's Atmosphere," *J. Quant. Spectroscopy and Radiative Transfer*, **60**, 943-961, 1998.
- Wellemeyer, C.G., *et al.*, "A correction for total ozone mapping spectrometer profile shape errors at high latitude," *J. Geophys. Res.*, **102**, 9029-9038, 1997.
- Yang, K., N. A. Krotkov, A. J. Krueger, S. A. Carn, P. K. Bhartia, and P. F. Levelt (2007), Retrieval of large volcanic SO₂ columns from the Aura Ozone Monitoring Instrument: Comparison and limitations, *J. Geophys. Res.*, 112, D24S43, doi:10.1029/2007JD008825.
- Young, A.T., "Rayleigh Scattering," *Appl. Opt.*, **20**, 533-535, 1981.
- Ziemke, J. R., S. Chandra & P.K. Bhartia, "Two New Methods of Deriving Tropospheric Column Ozone from TOMS Measurements: The Assimilated UARS MLS/HALOE and Convective Cloud Differential Technique," *J. Geophys. Res.*, **103**, 22,115-22,127, 1998.

Information on the TOMS and OMI total ozone algorithms is available in their ATBDs at

http://jwocky.gsfc.nasa.gov/version8/v8toms_atbd.pdf

and

http://www.knmi.nl/omi/documents/data/OMI_ATBD_Volume_2_V2.pdf

END OF DOCUMENT